


# Origin of active sites on silica–magnesia catalysts and control of reactive environment in the one-step ethanol-to-butadiene process

Received: 21 April 2022

Accepted: 9 March 2023

Published online: 17 April 2023

 Check for updates

Sang-Ho Chung<sup>1</sup>✉, Teng Li<sup>1</sup>, Tuiana Shoinkhorova<sup>1</sup>, Sarah Komaty<sup>1</sup>, Adrian Ramirez<sup>1</sup>, Ildar Mukhambetov<sup>1</sup>, Edy Abou-Hamad<sup>2</sup>, Genrikh Shterk<sup>1</sup>, Selvedin Telalovic<sup>1</sup>, Alla Dikhtiarenko<sup>1</sup>, Bart Sirks<sup>3</sup>, Polina Lavrik<sup>1</sup>, Xinqi Tang<sup>2</sup>, Bert M. Weckhuysen<sup>3</sup>, Pieter C. A. Bruijninx<sup>3,4</sup>, Jorge Gascon<sup>1</sup> & Javier Ruiz-Martínez<sup>1</sup>✉

Wet-kneaded silica–magnesia is a benchmark catalyst for the one-step ethanol-to-butadiene Lebedev process. Magnesium silicates, formed during wet kneading, have been proposed as the active sites for butadiene formation, and their properties are mainly explained in terms of the ratio of acid and base sites. However, their mechanism of formation and reactivity have not yet been fully established. Here we show that magnesium silicates are formed by the dissolution of Si and Mg subunits from their precursors, initiated by the alkaline pH of the wet-kneading medium, followed by cross-deposition on the precursor surfaces. Using two individual model systems (Mg/SiO<sub>2</sub> and Si/MgO), we demonstrate that the location of the magnesium silicates (that is, Mg on SiO<sub>2</sub> or Si on MgO) governs not only their chemical nature, but also the configuration of adsorbed ethanol and resulting selectivity. By using an NMR approach together with probe molecules, we demonstrate that acid and basic sites in close atomic proximity (~5 Å) promote butadiene formation.

1,3-Butadiene (hereafter butadiene) is a key monomer in the polymer industry. It is used for various end products, including polybutadiene rubber, styrene-butadiene rubber and acrylonitrile-butadiene rubber<sup>1,2</sup>. Currently, butadiene is mainly produced as a by-product of naphtha steam cracking, which is a process used for ethylene and propylene production. Correspondingly, the price of butadiene fluctuates with the supply–demand chain for ethylene<sup>3</sup>. This issue is exacerbated by the exploitation of shale gas, which leads to shortages in butadiene supply<sup>1,4,5</sup>. Moreover, these routes are fossil-based and clearly not

sustainable. The development of an alternative and more sustainable production process for butadiene is therefore needed. The Lebedev process, a process developed in the 1930s in which ethanol is converted into butadiene in a single catalytic reactor, is thus again receiving much attention as part of the value chain of both bioethanol production<sup>2,3,5–8</sup> and the more recent, cutting-edge processes that convert CO<sub>2</sub> into ethanol<sup>9–11</sup>.

Silica–magnesia has long been a benchmark catalyst in the Lebedev process as it was first used in the industrial process in the 1940s

<sup>1</sup>KAUST Catalysis Center (KCC), King Abdullah University of Science and Technology, Thuwal, Saudi Arabia. <sup>2</sup>Core Labs, King Abdullah University of Science and Technology, Thuwal, Saudi Arabia. <sup>3</sup>Inorganic Chemistry and Catalysis Group, Debye Institute for Nanomaterials Science, Utrecht University, Utrecht, the Netherlands. <sup>4</sup>Organic Chemistry and Catalysis Group, Debye Institute for Nanomaterials Science, Utrecht University, Utrecht, the Netherlands. ✉e-mail: [sangho.chung@kaust.edu.sa](mailto:sangho.chung@kaust.edu.sa); [javier.ruizmartinez@kaust.edu.sa](mailto:javier.ruizmartinez@kaust.edu.sa)

and shows stable catalytic performance<sup>12</sup>. The method used for the preparation of silica–magnesia catalysts considerably influences its catalytic performance, and among the methods studied, wet kneading yields the most active catalysts<sup>3,13</sup>. This superior performance has been attributed to the formation of distinct magnesium silicates<sup>14–16</sup>. Wet kneading is typically performed using solid precursors (for example, SiO<sub>2</sub> and Mg(OH)<sub>2</sub>) in water with continuous mixing (Fig. 1a)<sup>17</sup>. Various research efforts have aimed to achieve higher butadiene yields by optimizing the synthesis of wet-kneaded silica–magnesia catalysts. Several synthetic variables, such as the types of Si and Mg precursors<sup>17,18</sup>, the precursor morphology<sup>19</sup> and the Si/Mg ratio, have been investigated<sup>17,20</sup>. Post-synthetic factors, such as calcination, have also been shown to be important, as these alter the chemical structure of the formed magnesium silicates and therefore the catalytic performance<sup>21</sup>. However, all studies concluded that the optimal catalyst for the Lebedev process must strike a delicate balance between the number of acidic and basic sites<sup>8,13–15,17,18,21–24</sup>.

However, even after more than 70 years, the fundamental details of how wet kneading generates the active sites for butadiene formation and the corresponding silica–magnesia phases have not been fully elucidated. Studies have commonly considered the catalytic sites of wet-kneaded silica–magnesia for the Lebedev process to be a combination of different oxide forms (bulk silica, magnesia and magnesium silicate species (Mg–O–Si)) and surface hydroxy groups<sup>16,25</sup>. However, the origin, location and nature of the active species in the Lebedev process are still open questions.

Here we provide a detailed insight into the genesis, location, nature and proximity of the active sites of a wet-kneaded silica–magnesia catalyst for the Lebedev process. By varying the duration of wet kneading, we observed how the pertinent magnesium silicates are formed from their Si and Mg precursors. Based on these observations, the traditional wet-kneading conditions were modified by altering the pH of the wet-kneading medium to selectively prepare the individual constituents of the wet-kneaded silica–magnesia catalyst, that is, Mg-decorated SiO<sub>2</sub> and Si-decorated MgO (Mg/SiO<sub>2</sub> and Si/MgO, respectively). Following this approach, we discovered that butadiene formation is optimal when acidic sites are surrounded by and in close proximity to basic sites at the single-particle level, while minimizing ethylene formation.

## Results

### Catalyst synthesis by wet kneading

Wet-kneaded silica–magnesia catalysts were prepared using spherical Stöber SiO<sub>2</sub> and platelet-shaped Mg(OH)<sub>2</sub> at a nominal Si/Mg molar ratio of 1.0 under the synthesis conditions previously optimized for high butadiene yield<sup>17,21</sup>. To better understand the wet-kneading process, we monitored the pH of the wet-kneading aqueous solution in situ over 72 h. A sharp, initial increase in pH to 10.4 (that is, in the first 2 min) was observed as a result of the dissolution of brucite (Mg(OH)<sub>2</sub> → Mg<sup>2+</sup> + 2OH<sup>-</sup>), which initiates the wet-kneading process (Fig. 1b). The pH of the wet-kneading solution then gradually decreased to 9.2 and stabilized after 10 h of wet kneading. Elemental analysis by inductively coupled plasma optical emission spectrometry (ICP-OES) showed the Si/Mg molar ratio in solution to follow the same trend as the pH (exponential decay with wet-kneading time), while the same Si/Mg ratio in the solid state remained consistent over a period of 80 h (Fig. 1c,d). This suggests that the increase in hydroxide ions during the initial stage of the wet-kneading process triggers the dissolution of surface Si species of SiO<sub>2</sub>, which subsequently redeposit and form magnesium silicate composites<sup>26</sup>.

Even though the rapid variation in pH occurs only at the onset of the process (Fig. 1b, inset), we observed that wet kneading is a dynamic process and that the reaction continues to proceed after the pH has plateaued. Specifically, not only Si, but also Mg species continuously dissolve out from Mg(OH)<sub>2</sub>, as confirmed by elemental analysis

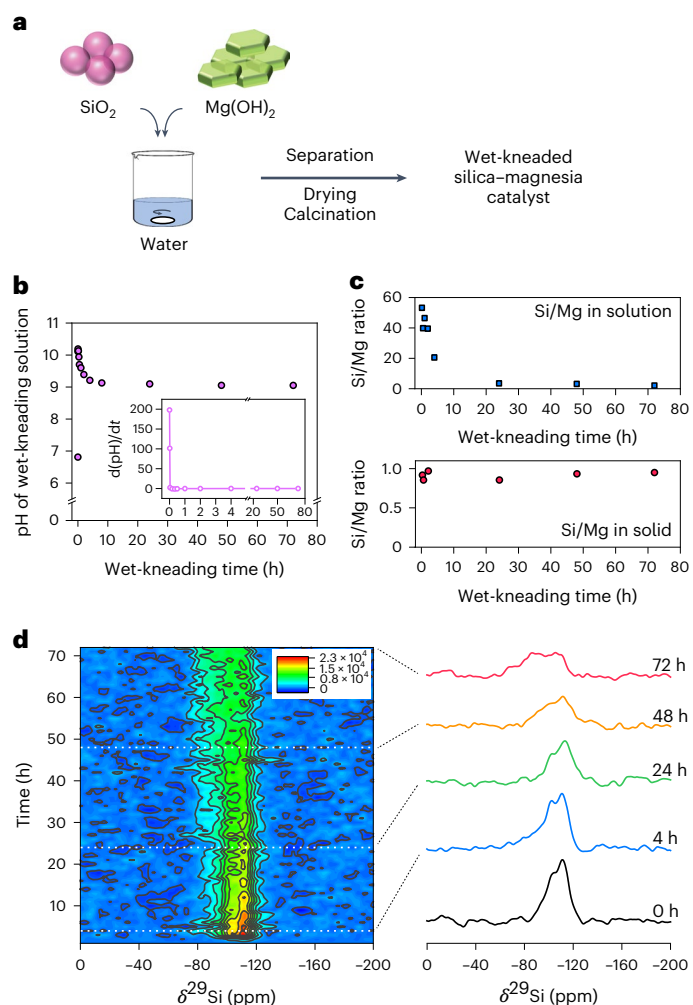


**Fig. 1 | Wet-kneading approach and time-resolved characterization of the silica–magnesia catalyst during wet kneading.** **a**, Schematic illustration of the synthesis of a wet-kneaded silica–magnesia catalyst from spherical SiO<sub>2</sub> and platelet-shaped Mg(OH)<sub>2</sub>. The x axis label of the main plot applies to the inset. **b**, Variation in the pH of the wet-kneading solution over 72 h. **c**, Molar ratio of Si and Mg in the wet-kneading solution and the resulting solids over time, determined by ICP-OES. **d**, In situ <sup>29</sup>Si direct-excitation NMR spectra of a silica–magnesia sample during 72 h of wet kneading.

(Supplementary Figs. 1 and 2 and Supplementary Note 1). The dissolved Si and Mg subunits can precipitate on the surfaces of Mg(OH)<sub>2</sub> and SiO<sub>2</sub>, respectively, as a result of the opposite surface charges on these species in this pH range (cross-deposition)<sup>17</sup>. Interestingly, the effect of longer-term wet kneading (that is, the dynamism of the wet-kneading process) can be inferred from studies on cement and concrete, where changes in similar systems (hydrated magnesium–silicate materials) have been investigated on timescales of a year<sup>27–29</sup>. For example, Roosz et al. conducted the long-term synthesis of MgO–SiO<sub>2</sub>–H<sub>2</sub>O for 1 year and obtained materials containing poorly crystalline magnesium silicates without pristine phases of SiO<sub>2</sub> and MgO (ref. 30). This result suggested the continuous dissolution and deposition of Si and Mg throughout the experiments.

Further insight into the wet-kneading process was obtained in situ using solid-state <sup>29</sup>Si NMR spectroscopy (Fig. 1d). As wet kneading starts immediately after mixing SiO<sub>2</sub> and Mg(OH)<sub>2</sub> in water (Fig. 1b), the <sup>29</sup>Si NMR spectrum of the physical mixture of SiO<sub>2</sub> and Mg(OH)<sub>2</sub> without water is labelled as *t* = 0. The <sup>29</sup>Si NMR spectrum at *t* = 0 shows three signals at –110, –100 and –91 ppm, which are attributed to siloxane groups (Q<sup>+</sup>, (SiO)<sub>4</sub>–Si), simple silanol (Q<sup>3</sup>, (SiO)<sub>3</sub>–Si–OH) and geminal

silanol ( $Q^2$ ,  $(SiO)_2-Si-(OH)_2$ ), respectively<sup>31,32</sup>. Upon wet kneading, the  $Q^4$  resonance continuously decreases and the  $Q^2$  and  $Q^3$  resonances gradually broaden. In addition, new features appear in the downfield region from  $-60$  to  $-90$  ppm (vide infra). This is in line with the notion above that the wet-kneading method evolves to a pseudo-steady state in which not only the dissolution of Si species from  $SiO_2$  nanoparticles (for Mg, vide infra), but also the subsequent formation of new magnesium silicate species is continuous (Supplementary Fig. 3 and Supplementary Table 1). Note that, in our study, the siloxane signal is still the most prominent after 72 h of wet kneading, showing that most of the bulk  $SiO_2$  remains unreacted. The powder X-ray diffraction (PXRD) patterns of the wet-kneaded silica–magnesia catalysts also show that the bulk structure of the  $SiO_2$  and  $Mg(OH)_2$  precursors remains (Supplementary Fig. 4).

To investigate the deposited Si and Mg species on the nanoscale, high-angle annular dark-field scanning transmission electron microscopy (HAADF-STEM) with energy-dispersive X-ray spectrometry (EDX) was used to characterize a silica–magnesia catalyst isolated after 10 min of wet kneading (WK-10min-dried; Fig. 2a–g). The STEM–EDX images show the precursor  $SiO_2$  and  $Mg(OH)_2$  particles to be well mixed and in close contact (Fig. 2a,b), which has been reported to be beneficial for the Lebedev process owing to the intimate interactions of the two components<sup>17</sup>. The high-magnification STEM–EDX images of the WK-10min-dried catalyst show that isolated Si clusters are deposited on the surface of  $Mg(OH)_2$  (Fig. 2c–f). This was further confirmed by the EDX area profile clearly showing the surface deposition of Si on  $Mg(OH)_2$  (Fig. 2g), which is in line with silicon-rich surfaces on a wet-kneaded silica–magnesia catalyst determined by low-energy ion scattering analysis<sup>25</sup>. While not as evident as the Si deposition on  $Mg(OH)_2$ , Mg species were also found on the  $SiO_2$  domains (Supplementary Fig. 5), indicating the deposition of dissolved Mg subunits on  $SiO_2$ . The decreased crystallinity of  $Mg(OH)_2$  after wet kneading observed by PXRD also suggests the dissolution of Mg subunits from brucite layers with the cross-deposition of Si subunits (Supplementary Fig. 4b and Supplementary Table 2).

The surface Si species on the dried catalysts were characterized in detail by NMR spectroscopy. Due to the poor signal from the surface Si species, dynamic nuclear polarization (DNP) surface-enhanced NMR spectroscopy (SENS) was used as it is a powerful and surface-sensitive technique for the identification of chemical structures<sup>33</sup>. Figure 2h shows the DNP-enhanced  $^1H$ - $^{29}Si$  cross-polarization (CP) magic-angle-spinning (MAS) NMR spectra of pristine  $SiO_2$  and wet-kneaded silica–magnesia samples at two wet-kneading times (10 min and 48 h) after drying. Notably, a distinct  $^{29}Si$  NMR resonance is observed at  $-66$  ppm after wet kneading. The  $^{29}Si$  NMR isotropic chemical shifts in silicates are related to the degree of anion condensation and the number of neighbouring silicon–oxygen tetrahedra<sup>34–36</sup>. We attribute this band to surface silicon species surrounded by magnesium cations (individual  $Q^0$  supported on  $Mg(OH)_2$ ), similarly to the  $Q^0$  silicate observed in tricalcium silicate (Supplementary Note 2)<sup>36</sup>. The formation of dimeric and trimeric Si species (at around  $-77$  and  $-84$  ppm, respectively) is also observed, especially for the WK-10min-dried sample. During the wet kneading for 48 h, the silicate units on brucite have progressively grown into longer silicate chains (oligomeric silicate species), showing upfield  $^{29}Si$  signals at chemical shifts beyond  $-86$  ppm (Fig. 2h, inset). The decrease in the  $Q^2/Q^4$  intensity ratio upon wet kneading (from 1.85 to 1.70) indicates that silanol groups are consumed, which can be related to the formation of surface magnesium silicates. Additionally, the resonances at  $-100$  ppm for WK-10min-dried and WK-48h-dried are shifted downfield by  $-1$  ppm after wet kneading, indicating the overlap of silica  $Q^3$  species ( $-100$  ppm) with the newly formed magnesium silicates, for example, talc ( $-98$  ppm)<sup>37</sup> and lizardite ( $-94$  ppm)<sup>38</sup>.

### Effect of thermal treatment

Catalyst calcination is a prerequisite to convert the dried, as-prepared material into an activated catalyst. We calcined the WK-10min-dried

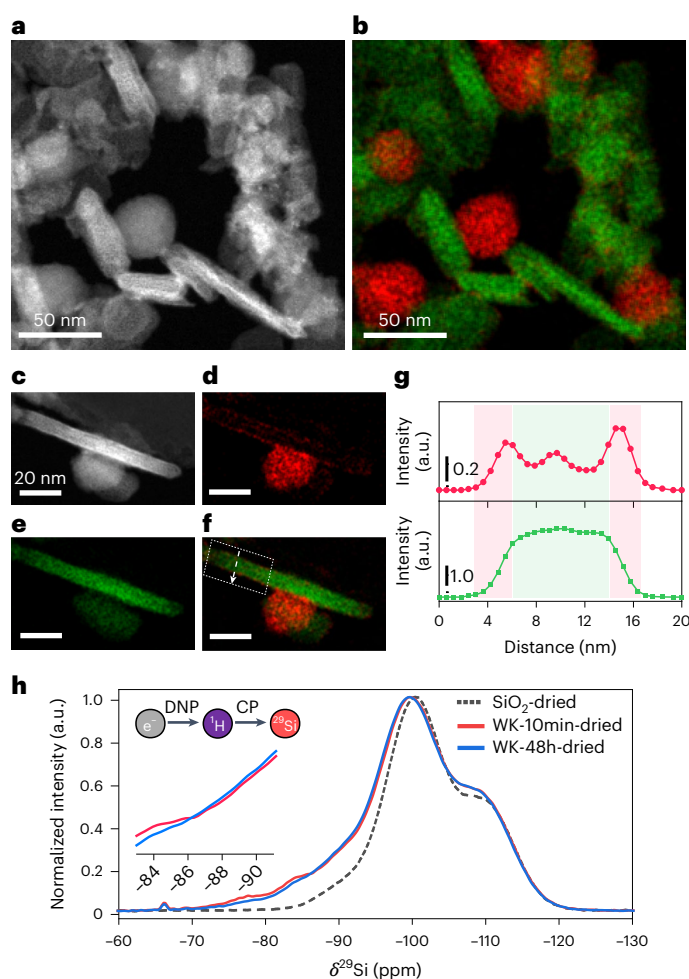


**Fig. 2 | Location and type of magnesium silicates on a wet-kneaded, dried catalyst.** a–f, HAADF-STEM image (a), the corresponding STEM–EDX elemental map from the sum of elemental maps of Si and Mg (b) and magnified HAADF-STEM image (c) and STEM–EDX maps (d–f) of the WK-10min-dried catalyst (Si and Mg are shown in red and green, respectively). The scale bar in c (20 nm) applies to all images in c–f. g, EDX area profiles of Si (red) and Mg (green) along the arrow shown in f. The red and green shadings are added to guide the location of Si at the edge and the centre of the  $Mg(OH)_2$ , respectively. h, DNP-enhanced  $^1H$ - $^{29}Si$  CP MAS NMR spectra of pristine  $SiO_2$  and two wet-kneaded silica–magnesia catalysts (WK-10min-dried and WK-48h-dried) after drying. The x axis label of the main plot applies to the inset.

catalyst at  $500$  °C for 5 h, the optimal conditions for obtaining high butadiene yields<sup>21</sup>. Fig. 3a,b shows the morphological differences between the wet-kneaded silica–magnesia catalyst before and after calcination. After calcination, the  $MgO$  surfaces show substantially corrugated nanopatterns with intervals of  $\sim 3$  nm between Si motifs (Supplementary Fig. 6). These patterns are not observed in the HAADF-STEM images of WK-10min-dried or a physical mixture of pristine  $SiO_2$  and  $Mg(OH)_2$  after calcination (Supplementary Figs. 6 and 7), suggesting that the final morphology of the  $MgO$  phase is largely influenced by the Si species deposited on  $Mg(OH)_2$  during wet kneading and subsequent calcination.

Further insight into the chemistry of the hydroxy groups was provided by thermal gravimetric analysis (TGA). TGA of dried samples of pristine  $SiO_2$  and  $Mg(OH)_2$  and wet-kneaded silica–magnesia revealed two distinct mass losses associated with (1) the removal of physisorbed water at approximately  $100$  °C and (2) the surface dehydroxylation of silica and/or magnesium hydroxide at  $300$ – $400$  °C (Fig. 3c and Supplementary Fig. 8)<sup>39</sup>. There was more physisorbed water in the dried  $SiO_2$



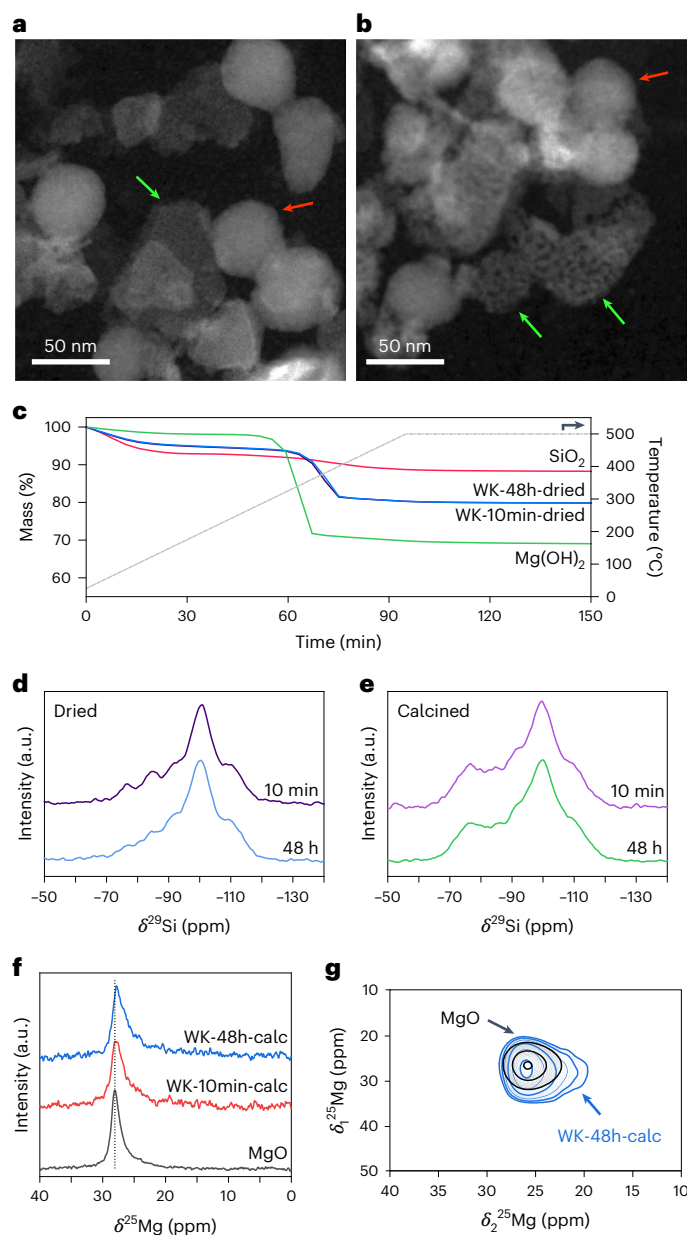


**Fig. 3 | Characterization of wet-kneaded silica–magnesia catalysts before and after calcination. a, b**, HAADF-STEM images of WK-10min-dried (**a**) and WK-10min-calc (**b**). SiO<sub>2</sub> and MgO particles are marked with red and green arrows, respectively. **c**, TGA analysis of dried pristine samples of SiO<sub>2</sub>, Mg(OH)<sub>2</sub> and the silica–magnesia catalyst after different wet-kneading times (10 min and 48 h). **d, e**, <sup>1</sup>H–<sup>29</sup>Si CP MAS NMR spectra of WK-10min-dried (**d**) and WK-48h-dried (**e**) before and after calcination. **f**, 1D <sup>25</sup>Mg direct-excitation MAS NMR spectra of MgO, WK-10min-calc and WK-48h-calc. **g**, 2D <sup>25</sup>Mg 3Q MAS NMR spectra of MgO (black lines) and WK-48h-calc (blue lines).

than in the dried Mg(OH)<sub>2</sub> (7.1% and 1.9%, respectively), which explains why the actual ratios of Si/Mg in the wet-kneaded silica–magnesia samples were slightly less than 1.0 (0.91 by ICP-OES, Fig. 1c). Notably, modification of the Mg(OH)<sub>2</sub> surface with Si species considerably hindered the dehydroxylation of Mg(OH)<sub>2</sub>, shifting the onset and offset temperatures by –40 °C (Supplementary Fig. 8 and Supplementary Note 3). This was also observed in complementary in situ PXRD measurements (Supplementary Fig. 8). The phase transformation from Mg(OH)<sub>2</sub> to the dehydroxylated MgO periclase phase starts in the external surface layers of the particles<sup>40,41</sup> and is influenced by the substitutional atoms on the Mg(OH)<sub>2</sub> surface<sup>42</sup>. We expect that the smaller

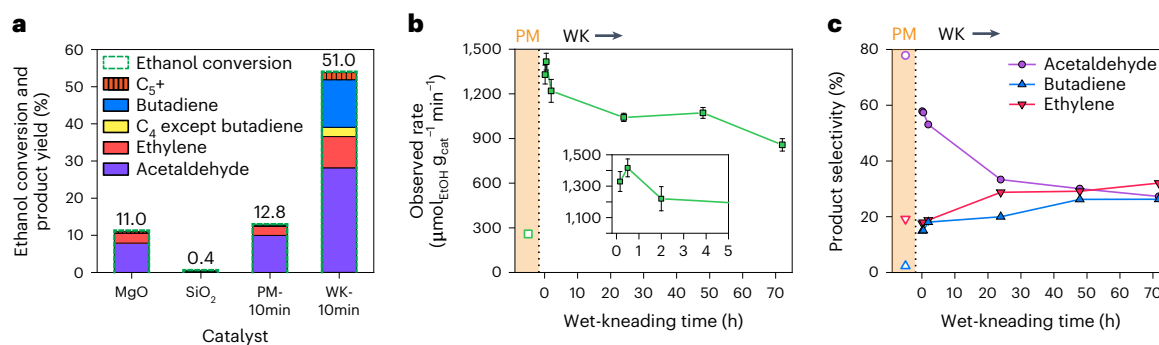
Si<sup>4+</sup> ions (ionic radius,  $r_{\text{ion}}$ , of Si<sup>4+</sup> and Mg<sup>2+</sup> = 0.026 and 0.072 nm, respectively<sup>43</sup>) observed on the surface of Mg(OH)<sub>2</sub> in WK-10min-dried (Fig. 2) retard the surface dehydroxylation of Mg(OH)<sub>2</sub> (refs. 44,45), creating the corrugated surface structure observed by electron microscopy (Fig. 3b and Supplementary Fig. 7).

Figure 3d,e shows the <sup>1</sup>H–<sup>29</sup>Si CP MAS NMR spectra of wet-kneaded silica–magnesia catalysts before and after calcination. Numerous types of magnesium silicate are found in nature<sup>46</sup> and show distinct <sup>29</sup>Si NMR signals, reflecting the local silicon environments (Supplementary Fig. 3)<sup>34,47</sup>. For example, phyllosilicates, pyroxenes and olivines show characteristic features at around –85 to –100 ppm (refs. 17,38,48,49), –75 to –90 ppm (refs. 34,47) and –60 to –75 ppm (refs. 48,50,51), respectively. Amorphous magnesium silicates also exhibit <sup>29</sup>Si NMR features over a wide range, from –70 to –95 ppm (refs. 48,50,52–54). In the wet-kneaded samples, the resonance at –77 ppm is considerably enhanced after calcination, indicating that the proton density around the <sup>29</sup>Si nucleus of this magnesium silicate is rather high<sup>21</sup>. We assign this feature to the dimeric Q<sup>1</sup> species in the MgO domain, which contains hydroxy groups situated between Si and Mg species to compensate the negatively charged oxygen anions induced by the incorporation of Si<sup>4+</sup> into the periclase phase (Mg<sup>2+</sup>–O<sup>2-</sup>). The resonances at –84, –93 and –97 ppm are contributions from enstatite<sup>17,48,50</sup> and lizardite-type<sup>38,39</sup> and talc-type phyllosilicates<sup>17,48</sup>, respectively.

The chemistry of the Mg species was also directly investigated by <sup>25</sup>Mg NMR spectroscopy. Unlike <sup>29</sup>Si NMR spectroscopy, the number of <sup>25</sup>Mg NMR studies performed on magnesium silicates is rather limited owing to the intrinsic insensitivity (0.26% to <sup>1</sup>H) and relatively low natural abundance (10%) of <sup>25</sup>Mg (refs. 38,55,56). Combined with its quadrupolar nature ( $I = 5/2$ ) with low Larmor frequency (6% to <sup>1</sup>H), the acquisition and interpretation of <sup>25</sup>Mg NMR spectra is indeed rather complex. Recent advances in solid-state NMR spectroscopy, such as the availability of higher magnetic fields and the use of signal enhancement pulse sequences, offer new opportunities for <sup>25</sup>Mg NMR studies<sup>56</sup>. This prompted us to consider natural-abundance solid-state <sup>25</sup>Mg NMR spectroscopy at high magnetic fields (21.1 T) as a tool for understanding the wet-kneaded silica–magnesia catalysts. One-dimensional (1D) <sup>25</sup>Mg NMR spectra are shown in Fig. 3f and Supplementary Fig. 9. The Mg sites in pristine MgO are highly symmetric (cubic symmetry,  $Fm\bar{3}m$ )<sup>57</sup>, showing a single symmetrical resonance at 26.3 ppm. After wet kneading, the <sup>25</sup>Mg signals of the silica–magnesia catalysts shift slightly upfield with asymmetrical broadening, indicating the possible formation of new Mg sites in the wet-kneaded silica–magnesia catalysts. We performed natural-abundance <sup>25</sup>Mg triple-quantum (3Q) MAS experiments for MgO and WK-48h-calc (Fig. 3g, Supplementary Fig. 10 and Supplementary Table 3). While pristine MgO shows a symmetrical <sup>25</sup>Mg environment (isotropic chemical shift,  $\delta_{\text{iso}} = 26.3$  ppm), the WK-48h-calc catalyst exhibits an asymmetrically broadened feature with a relatively large quadrupole coupling constant ( $C_Q = 1.3$  MHz), next to the symmetrical signal from MgO. We attribute the broad <sup>25</sup>Mg feature of the WK-48h-calc catalyst to structurally disordered Mg species<sup>58–60</sup>, induced by incorporating Si<sup>4+</sup> into the MgO periclase, that is, the deviation from the site symmetry of the MgO octahedral structure.

### Catalytic performance at different wet-kneading times

Figure 4 shows the catalytic activity of the pristine materials (SiO<sub>2</sub> and MgO) and wet-kneaded silica–magnesia catalysts obtained after different wet-kneading times. Over the investigated timespan (~40 h), wet-kneaded silica–magnesia samples did not show any significant deactivation (Supplementary Fig. 11). Pristine SiO<sub>2</sub> and MgO and their physical mixture showed limited catalytic performance, not only in the conversion rate of ethanol, but also in their selectivity towards butadiene (Fig. 4a), in agreement with previous results<sup>15,18</sup>. For example, pristine Stöber SiO<sub>2</sub> showed no catalytic activity in the Lebedev process, whereas MgO produced butadiene at very low rates (3.1 μmol<sub>butadiene</sub> g<sub>cat</sub><sup>–1</sup> min<sup>–1</sup>).



**Fig. 4 | Catalytic performances of wet-kneaded silica–magnesia catalysts at different wet-kneading times.** **a**, Ethanol conversion and product yields observed for pristine MgO and SiO<sub>2</sub>, a catalyst prepared by physical mixing of SiO<sub>2</sub> and Mg(OH)<sub>2</sub> for 10 min (PM) and a silica–magnesia catalyst after wet kneading for 10 min. **b**, Ethanol conversion rate for PM and silica–magnesia catalysts at different wet-kneading times. The data are presented as mean ± s.d. of measurements performed in triplicate. Reaction conditions for **a** and **b**: 50 μl

catalyst, LHSV 1.0 h<sup>-1</sup> (WHSV 7.3 h<sup>-1</sup>), 425 °C. The x axis label of the main plot applies to the inset. **c**, Product selectivity of PM and wet-kneaded silica–magnesia catalysts at isoconversion (ethanol conversion: 12.8% and 14.8 ± 0.8% for PM and wet-kneaded samples, respectively). The product selectivity was calculated from activity measurements at 15 h on stream. Reaction conditions for **c**: 20 μl catalyst, LHSV 2.0–3.75 h<sup>-1</sup> (WHSV 14.6–27.0 h<sup>-1</sup>), 425 °C. All samples were dried and calcined before reaction.

This indicates that the multiple reaction steps towards butadiene occur to a limited extent on the intrinsic acidic and basic sites on the pristine MgO surface (Supplementary Fig. 14). Similarly, Hayashi et al. observed negligible ethanol conversion on SiO<sub>2</sub> and ~40 times lower butadiene formation rates on MgO compared with a metal-promoted phyllosilicate (Zn-talc)<sup>61</sup>. Although the mechanism of the Lebedev process is under discussion<sup>4,8,62–64</sup>, the most plausible mechanism involves ethanol dehydrogenation to acetaldehyde, aldol condensation between two acetaldehyde molecules to form 3-hydroxybutanal (acetaldo), subsequent dehydration and hydrogenation steps to yield crotonaldehyde and crotyl alcohol, respectively, and finally intramolecular dehydration to yield butadiene<sup>2,4,5</sup>. Based on the observed high selectivity towards acetaldehyde but low selectivity towards butadiene, we expect that pristine MgO (and the corresponding physical mixture of MgO and SiO<sub>2</sub> catalyst) does not provide sufficient catalytic sites for the initial dehydrogenation step nor the appropriate active sites for the production of butadiene. Meanwhile, compared with the physical mixture of MgO and SiO<sub>2</sub>, the silica–magnesia catalyst obtained after only 10 min of wet kneading resulted in a fourfold increase in ethanol conversion rate and a sevenfold increase in butadiene selectivity (Fig. 4b,c). This clearly suggests that the cross-deposition resulting from wet kneading allows for the interplay of the acidic and basic sites needed for the multiple reaction steps leading to butadiene from ethanol<sup>13,16,65</sup>.

However, the catalyst transformations during wet kneading are not necessarily beneficial for the Lebedev process (Fig. 4b,c). For example, the ethanol conversion rate gradually decreased and had fallen by 20% after 72 h of wet kneading and ethylene selectivity increased, which is an unwanted by-product. This detrimental effect of prolonged wet kneading on the efficiency of the Lebedev process was not expected as more magnesium silicates are formed and dispersed over the catalyst surface in extended dissolution and cross-deposition compared with in shorter wet-kneading times (Supplementary Fig. 12); therefore, more ethanol should be converted to butadiene over these magnesium silicates. A textural effect can be ruled out as the Brunauer–Emmett–Teller (BET) specific surface area of the wet-kneaded catalysts remains nearly the same for different wet-kneading times (Supplementary Fig. 13).

Balanced acidic and basic sites have often been proposed to be key to obtaining higher yields of butadiene<sup>3,4,713,16–18,21,25,66,67</sup>. For example, in the two-step ethanol-to-butadiene process on beta-zeolite catalysts, a dependency was observed between the ratio of acidic and basic sites and butadiene selectivity (the highest butadiene selectivity was observed at the acid/base ratio of ~1.2)<sup>68</sup>. We characterized the

wet-kneaded silica–magnesia catalysts by temperature-programmed desorption (TPD) using ammonia and carbon dioxide as probe molecules to determine the number of acidic and basic sites on the catalysts, respectively, (Supplementary Fig. 14). The acidity–basicity characterization revealed a ‘general’ trend in ethanol conversion, that is, the catalysts with an acid/base ratio of around 2 showed high ethanol conversion, whereas those with a ratio higher than 4 gave low ethanol conversion. However, this analysis does not provide a clear picture of the role of the acidic and basic sites of wet-kneaded silica–magnesia catalysts in the Lebedev process and the corresponding butadiene selectivity. A recent study by Szabo et al. also reflected the difficulty in determining a clear relationship between acid–base sites and catalytic performance in the Lebedev process<sup>69</sup>. All these results suggest that not all magnesium silicates are beneficial for butadiene production and/or that the spatial distribution of the active sites is not adequate for the multi-step catalytic reaction.

### Rational design of two model components in wet-kneaded catalysts

As seen above, wet kneading generates active sites by providing an environment for simultaneous dissolution and cross-deposition of Si and Mg to ultimately give a mixture of two particles with contrasting catalyst surfaces (for example, Mg on SiO<sub>2</sub> and Si on MgO). These heterogeneous features inherent in traditional wet-kneaded silica–magnesia catalysts hamper the establishment of direct structure–performance relationships for the Lebedev process. To disentangle these contributions, we modified the traditional wet-kneading method and prepared two model catalysts in which either SiO<sub>2</sub> or MgO is selectively decorated with Mg and Si (Mg/SiO<sub>2</sub> and Si/MgO), respectively (Fig. 5a). The materials were prepared in either ammonium nitrate or ammonium hydroxide solutions, which provide wet-kneading medium pH values of 8.3 or 11.4, respectively. At a pH of 8.3, the dissolution of SiO<sub>2</sub> is limited<sup>53,70</sup>, whereas the solubility of magnesium species is greatly enhanced by a factor of >10<sup>14</sup> with respect to pure Mg(OH)<sub>2</sub> owing to the formation of magnesium nitrate (solubility product constant,  $K_{sp}$ , for Mg(NO<sub>3</sub>)<sub>2</sub> and Mg(OH)<sub>2</sub> are  $K_{sp,Mg(NO_3)_2}$  and  $K_{sp,Mg(OH)_2} = 2.4 \times 10^{-3}$  and  $5.6 \times 10^{-12}$ , respectively<sup>71</sup>). In contrast, SiO<sub>2</sub> nanoparticles can completely dissolve at a pH of 11.4 (an approximate tenfold increase in solubility compared with at a pH of 7)<sup>72,73</sup>, while Mg(OH)<sub>2</sub> retains its morphological structure.

HAADF-STEM with EDX analysis confirmed the distinct nature of the two constituents: neither SiO<sub>2</sub> nor MgO was observed on the Si/MgO and Mg/SiO<sub>2</sub> model systems, respectively (Fig. 5a and Supplementary

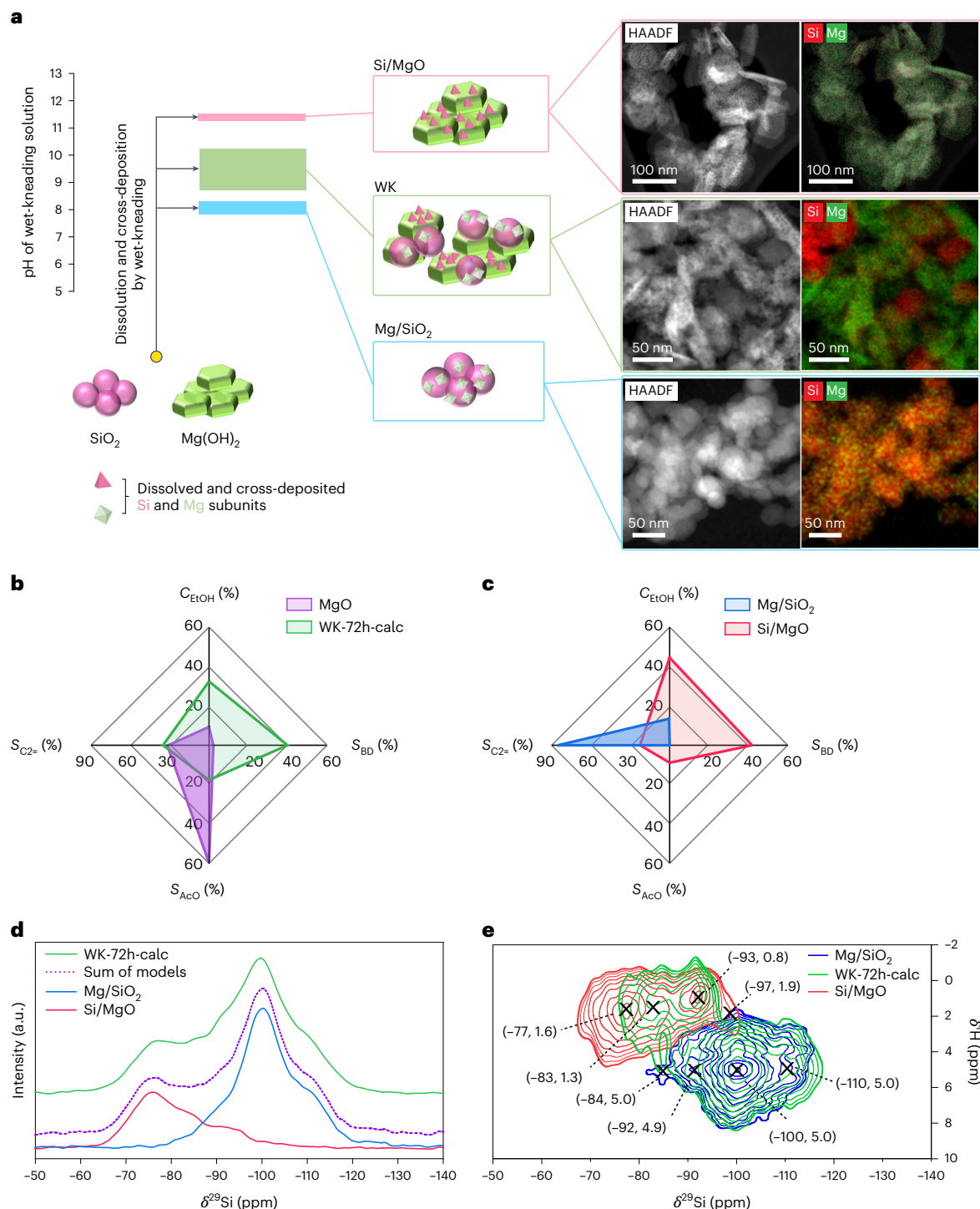


**Fig. 5 | Identification of the key surface magnesium silicates responsible for the one-step Lebedev process.** **a**, Schematic of the preparation of the model catalysts Mg/SiO<sub>2</sub> and Si/MgO by modified wet kneading. HAADF-STEM and EDX images of the calcined catalysts are included. **b,c**, Catalytic activity of MgO and WK-72h-calc (**b**) and Mg/SiO<sub>2</sub> and Si/MgO (**c**) in the conversion of ethanol. The plots show the conversion (*C*) and selectivity (*S*) towards ethylene (C2=),

acetaldehyde (AcO) and butadiene (BD). Reaction conditions: 50 μl catalyst, LHSV 1.0 h<sup>-1</sup> (WHSV 7.3 h<sup>-1</sup>), 425 °C. **d,e**, 1D <sup>29</sup>Si CP MAS NMR (**d**) and 2D <sup>29</sup>Si-<sup>1</sup>H CP frequency-switched Lee-Goldberg (FSLG) HETCOR spectra (**e**) of the WK-72h-calc, Si/MgO and Mg/SiO<sub>2</sub> catalysts. The values in parentheses in **e** represent (<sup>29</sup>Si, <sup>1</sup>H) chemical shifts. The intensities of the NMR spectra are normalized for clarity.

Fig. 15). PXRD analysis supported the above observation that pristine SiO<sub>2</sub> and MgO are not present in the corresponding model systems of Si/MgO and Mg/SiO<sub>2</sub>, respectively, whereas the wet-kneaded catalyst (WK-72h-calc) showed the presence of both pristine SiO<sub>2</sub> and MgO (Supplementary Fig. 16). The crystallite size of MgO in WK-72h-calc and Si/MgO was similar (8.3 and 8.4 nm, respectively), indicating that

the modified wet kneading alters only the surface of MgO by selective Si dissolution and deposition.

Figure 5b,c shows the catalytic performances of the two model catalysts as well as those of pristine MgO and the WK-72h-calc catalyst for comparison. The two model catalysts displayed contrasting catalytic activity, showing around three times higher ethanol



conversion activity on Si/MgO than on Mg/SiO<sub>2</sub>. In addition, the highest selectivity towards ethylene and butadiene was observed for the Mg/SiO<sub>2</sub> and Si/MgO catalysts, respectively, among all the catalysts tested in this study (under the conditions liquid hourly space velocity (LHSV) 1.0 h<sup>-1</sup>, weight hourly space velocity (WHSV) 7.3 h<sup>-1</sup> and 425 °C; a comparison of the product selectivity for the same level of conversion is shown in Supplementary Fig. 17a). Strikingly, the model Si/MgO catalyst showed a 36% higher butadiene production rate than the conventional wet-kneaded silica–magnesia catalysts (490 versus an average 358 μmol<sub>butadiene</sub> g<sub>cat</sub><sup>-1</sup> min<sup>-1</sup>) while minimizing rate of production of unwanted ethylene (272 versus an average 278 μmol<sub>ethylene</sub> g<sub>cat</sub><sup>-1</sup> min<sup>-1</sup>).

The chemical structures of the species on the Mg/SiO<sub>2</sub> and Si/MgO catalysts were investigated using <sup>29</sup>Si and <sup>25</sup>Mg NMR spectroscopy. Figure 5d,e shows the 1D <sup>1</sup>H–<sup>29</sup>Si CP MAS NMR spectra and two-dimensional (2D) <sup>1</sup>H–<sup>29</sup>Si CP FSLG heteronuclear correlation (HETCOR) spectra of the two model catalysts together with those of WK-72h-calc for comparison. The spectra show that a linear combination of the spectra of the two model catalysts closely resembles the spectral features of the traditional wet-kneaded silica–magnesia catalyst. For example, the Mg/SiO<sub>2</sub> catalyst shows <sup>29</sup>Si resonances from bulk SiO<sub>2</sub> (Q<sup>3</sup> and Q<sup>4</sup> at –100 and –110 ppm, respectively) with two additional peaks at –84 and –92 ppm, which are attributed to amorphous magnesium silicates (Q<sup>2</sup> (1Mg, 1OH, 2Si) and Q<sup>3</sup> (1Mg, 3Si), respectively)<sup>53</sup>. As seen from the PXRD patterns (Supplementary Fig. 16), the Mg species on the SiO<sub>2</sub> surface do not form crystalline-layered magnesium silicates owing to the lack of crystalline octahedral Mg<sup>2+</sup> layers. Interestingly, correlations between <sup>29</sup>Si and <sup>1</sup>H were mostly observed for silanols associated with physisorbed and hydrogen-bonded water (δ<sup>1</sup>H ≈ 5 ppm)<sup>74</sup>. Owing to the low Mg content in Mg/SiO<sub>2</sub> (2.6 wt% Mg), we used a quadrupolar Carr–Purcell–Meiboom–Gill pulse sequence combined with double-frequency sweeps (DFS–QCPMG) to enhance the <sup>25</sup>Mg signal intensity (Supplementary Fig. 18). Notably, Mg/SiO<sub>2</sub> showed a distinct <sup>25</sup>Mg resonance with a large quadrupolar constant (C<sub>Q</sub> = 2.6 MHz at δ<sub>iso</sub> = 15 ppm), indicating that the bonding geometries of the surface Mg species are considerably different from those of the Mg species in pristine MgO and the Si/MgO catalyst. The Mg/SiO<sub>2</sub> catalyst shows a remarkable increase in the number of acidic sites compared with the original SiO<sub>2</sub> material (Supplementary Fig. 14), suggesting that the isolated Mg species on the SiO<sub>2</sub> surface retain their acidic nature to favour ethylene formation.

The 1D <sup>1</sup>H–<sup>29</sup>Si CP MAS NMR spectrum of the Si/MgO catalyst shows four <sup>29</sup>Si resonances at –77, –85, –93 and –97 ppm with characteristic <sup>1</sup>H correlations (0.5 < δ<sup>1</sup>H < 2 ppm), attributed to structural hydroxy groups (Si–OH–Mg; Fig. 5d,e and Supplementary Fig. 19). Similar <sup>1</sup>H chemical shifts were observed for phyllosilicates when the hydroxy groups were part of the octahedral Mg layers but pointing towards the surface Si units<sup>75</sup>. Thus, we assign the resonances observed for the Si/MgO catalyst as hydrous magnesium silicates, for example, Q<sup>1</sup> (3Mg, 1Si), Q<sup>2</sup> (2Mg, 2Si), and lizardite- and talc-type Q<sup>3</sup> (1Mg, 3Si). The <sup>25</sup>Mg 3Q MAS NMR spectrum of the Si/MgO catalyst also suggests that some surface Mg species are decorated with deposited Si species, as was also observed for WK-48h-calc (Supplementary Fig. 10 and Supplementary Table 3). Furthermore, the NH<sub>3</sub> TPD data show that additional acidic sites are created on this catalyst, with around 20 and 3 times more acidic sites than pristine SiO<sub>2</sub> and MgO, respectively (Supplementary Fig. 14). These results, together with the electron microscopy measurements (Fig. 5a and Supplementary Fig. 15), indicate that new acidic sites are created in close proximity to a matrix of basic MgO sites by modified wet kneading.

To gain more accurate information on the proximity of acid and basic sites, we developed a spectroscopic titration method consisting of the co-adsorption of NH<sub>3</sub> and CHCl<sub>3</sub> on MgO and Si/MgO catalysts followed by 2D <sup>1</sup>H double-quantum single-quantum (DQ–SQ) MAS NMR spectroscopy<sup>76,77</sup>. More details about the conceptualization of

the method, experimental details, data analysis and validation of the adsorption of the probe molecules by Fourier transform infrared spectroscopy can be found in Supplementary Note 4 and Supplementary Figs. 20 and 21. This 2D correlation NMR technique, shown in Fig. 6a,b for MgO and Si/MgO, allows the study of the dipolar coupling interactions of a certain proton with other protons within a range of ~5 Å, which would be the distance between the protons of chemisorbed NH<sub>3</sub> and CHCl<sub>3</sub> on acid and basic sites, respectively. For the model Si/MgO catalyst, the <sup>1</sup>H chemical shifts of the adsorbed NH<sub>3</sub> on Brønsted and Lewis acid sites show self-correlations at 5.0 and –0.1 ppm, respectively. This indicates a greater density of acid sites on Si/MgO than on MgO, in line with the results of NH<sub>3</sub> TPD (Supplementary Fig. 14). After the adsorption of CHCl<sub>3</sub> on pristine MgO and Si/MgO, additional protons are observed at around 3.5 and 0.9 ppm, respectively, indicating that the proton in CHCl<sub>3</sub> can interact with the basic sites in various configurations (Supplementary Fig. 21)<sup>13</sup>. Notably, the acidic sites show correlations with the basic sites only for the Si/MgO catalyst (δ<sup>1</sup>H<sub>NH<sub>3</sub></sub> at 5.0 and –0.1 ppm and δ<sup>1</sup>H<sub>CHCl<sub>3</sub></sub> at 3.5 and 0.9 ppm, respectively). This suggests that Si modification of MgO (Si/MgO) creates additional acid sites and that these sites are within 5 Å of basic sites (Fig. 6c), which was not observed for the pristine MgO and PM catalysts. To investigate further the effect of acid–base proximity, we compared the catalytic performances of the WK-10min-calc, WK-30min-calc and Si/MgO samples, which have similar acid/base ratios but different acid–base proximities. The Si/MgO sample clearly showed an ~50% higher butadiene rate of formation than the wet-kneaded samples, in which a fraction of their acid and basic sites are physically separated (Supplementary Figs. 11 and 17). We also measured the catalytic performances of the two model catalysts (Si/MgO and Mg/SiO<sub>2</sub>) physically mixed in different ratios; the results clearly show that the physical mixtures are not able to achieve higher butadiene rate of formation (Supplementary Fig. 17b). All these results highlight the importance of acid and basic sites in close proximity for the Lebedev reaction.

### Mechanistic investigation using operando DRIFT–MS spectroscopy

Although the ethanol-to-butadiene reaction is generally considered to occur by an acid–base mechanism, the catalytic sites have not been identified. For example, the acidic and basic sites on wet-kneaded silica–magnesia catalysts have commonly been attributed to unsaturated Mg<sup>2+</sup>, as Lewis acid sites<sup>13,21</sup>, and MgO (and/or MgOH), as basic sites<sup>25,62</sup>, whereas other studies have reported surface silanol as weak Brønsted acid sites<sup>16,78</sup> and Si–O–Mg sites as basic sites<sup>13,78</sup>. Based on the two model systems where we can identify the contributions from each component (Mg/SiO<sub>2</sub> and Si/MgO), we investigated the structure–performance relationship and reaction mechanism of the Lebedev process by operando diffuse reflectance infrared Fourier transform spectroscopy (DRIFTS) coupled with mass spectrometry (MS). The DRIFTS spectra of the catalyst samples are shown in Fig. 6d. For the Mg/SiO<sub>2</sub> catalyst, compared with Si/MgO, the asymmetric CH<sub>3</sub> stretching of ethanol<sup>79,80</sup> is blueshifted to 2,984 cm<sup>-1</sup> during the reaction at 425 °C. This suggests that the orbitals of the CH<sub>3</sub> group are rehybridized upon adsorption on the surface of Mg/SiO<sub>2</sub> and that the H–C bond (in the CH<sub>3</sub> group) becomes more polarized<sup>81</sup> (that is, the partial positive charge on the H and the negative charge on the C increase). Thus, we expect that the CH<sub>3</sub> group interacts with the Mg–O–Si surface, where Mg<sup>2+</sup> acts as a Lewis acid site and stabilizes the carbanion (Supplementary Fig. 22a)<sup>62</sup>. This is supported by operando DRIFTS spectra, which show no evidence of interactions between the alcohol functional group and the hydroxy groups of the catalyst surface during the reaction (Supplementary Fig. 23). Thus, the dehydration of ethanol to ethylene is highly favoured on the isolated Mg units on SiO<sub>2</sub> (Fig. 5b), especially in the proximity of the acidic site (Mg<sup>2+</sup>) and conjugated base (Mg–O–Si). This is in line with the increased ethylene selectivity observed for catalysts containing more of the Mg/SiO<sub>2</sub> component, such as catalysts wet-kneaded

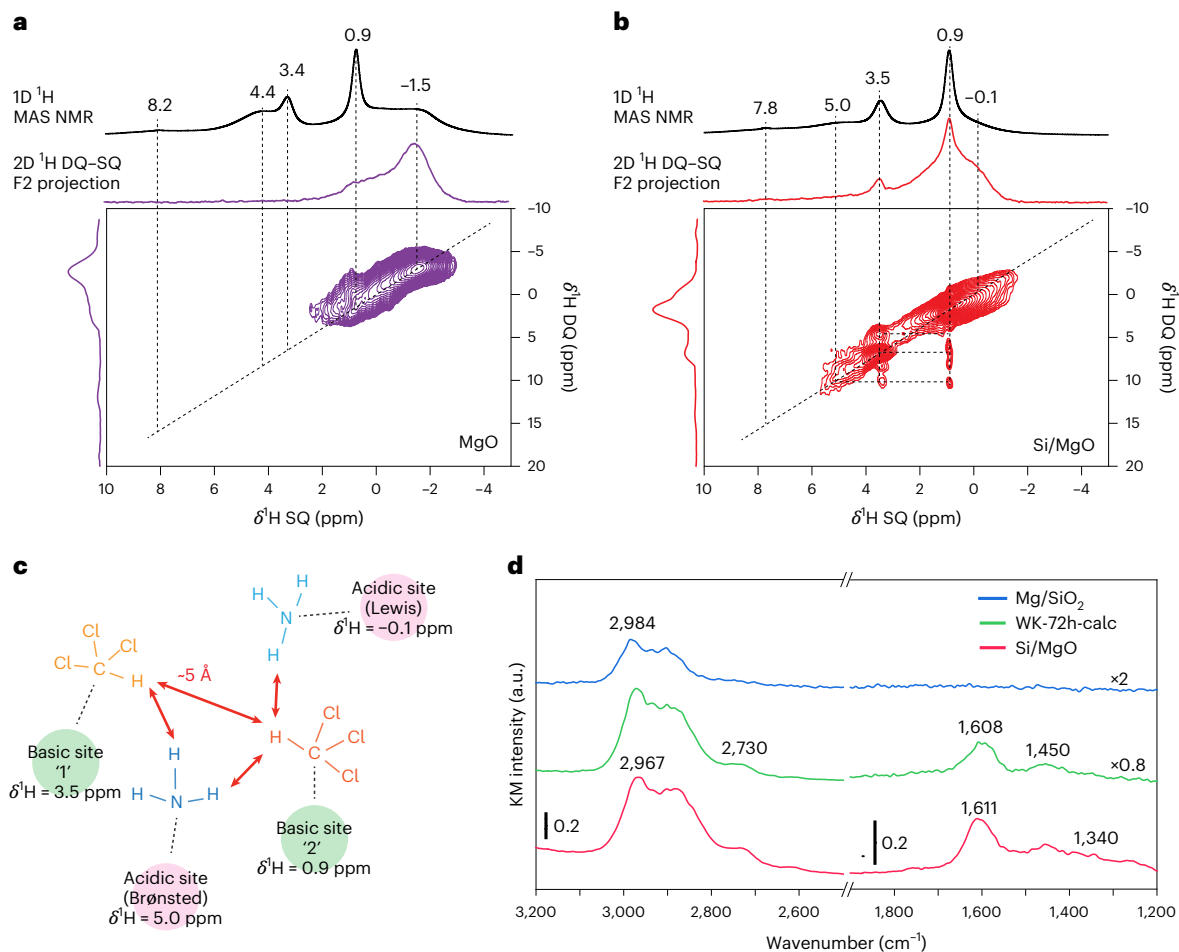


**Fig. 6 | Characterization of acid–base site proximity and formation of reaction intermediates.** **a, b**, 2D  $^1\text{H}$  DQ–SQ MAS NMR spectra of MgO (**a**) and Si/MgO (**b**). **c**, Schematic of acid–base proximity on the model Si/MgO catalyst based on the 2D  $^1\text{H}$  DQ–SQ MAS NMR data. **d**, Operando DRIFTS spectra in

Kubelka–Munk function (KM) acquired during continuous ethanol dosing on WK-72h-calc and the model catalysts at 425 °C. The intensities of the NMR and DRIFTS spectra are normalized for clarity.

for longer periods of time and the physical mixtures of Si/MgO and Mg/SiO<sub>2</sub> (Fig. 4c and Supplementary Fig. 17).

For Si/MgO and WK-72h-calc, which retain dispersed Si units on MgO, the surface hydroxy groups of the catalysts interact with ethanol and show a negative infrared band at  $-3,730\text{ cm}^{-1}$ , a band completely absent from the spectrum of the Mg/SiO<sub>2</sub> catalyst (Supplementary Fig. 23). This indicates a strong interaction with the terminal Si–OH–Mg groups of the Si/MgO surface (rather than Mg–OH, with an absorption band at  $3,749\text{ cm}^{-1}$ ; Supplementary Figs. 23 and 24 and Supplementary Note 5). Moreover, in the  $3,600\text{--}3,200\text{ cm}^{-1}$  region, a broad OH stretching band is observed, attributed to intermolecular hydrogen bonding of ethanol with the catalyst surface. We expect that the interactions previously observed in DRIFTS studies between the reactants and/or intermediates and the surface hydroxy groups on wet-kneaded silica–magnesia catalysts<sup>62,66,78,82</sup> can indeed be attributed to the Si/MgO surface (Si–OH–Mg). Notably, an additional infrared band is observed at  $2,730\text{ cm}^{-1}$  (Fig. 6d), which is attributed to the asymmetric stretching of the C–H bond at the  $\alpha$ -carbon of the adsorbed ethanol<sup>82</sup>. Taken together with the rapid formation of H<sub>2</sub> on the Si/MgO catalyst (Supplementary Fig. 25), we expect that heterolytic elimination of hydrogen from ethanol is favoured<sup>13,83–90</sup> and consequently that acetaldehyde is preferably produced (Supplementary Fig. 22b). Although the assignment of the bands in the range  $1,700\text{--}1,200\text{ cm}^{-1}$  is cumbersome and they have been attributed to intermediates (for example, surface acetates)<sup>66,91–94</sup> or the overlap of several vibration modes of

CH<sub>x</sub> or OCO(H) species<sup>82,95,96</sup>, the infrared feature at  $-1,611\text{ cm}^{-1}$  is clearly observed for Si/MgO (and WK-72h-calc) and attributed to C=C stretching of key intermediate species such as crotyl alcohol (Fig. 6d)<sup>62,78</sup>. For the Mg/SiO<sub>2</sub> model catalyst, these infrared features of intermediates towards butadiene are not observed, which is in line with its low butadiene selectivity. We additionally performed a DRIFTS–MS study on pristine MgO and Si/MgO catalysts under temperature-programmed surface reaction (TPSR) conditions (Supplementary Fig. 26). In neither case did we observe the characteristic infrared bands and MS spectra of the crotonaldehyde and crotyl alcohol intermediates due to their subsequent rapid dehydration to butadiene under the reaction conditions<sup>94,97</sup>. The spectral features of both samples at 50 °C are similar, but with different intensity ratios. At high temperature, the infrared bands of acetaldehyde at  $3,020$  and  $2,793\text{ cm}^{-1}$  (CH<sub>3</sub> and CH stretching, respectively)<sup>62,66</sup> are more predominant on the MgO surface than on Si/MgO. This suggests that acetaldehydes are strongly adsorbed and stabilized on the Mg<sup>2+</sup>–O<sup>2-</sup> pair in the horizontal configuration<sup>98,99</sup>, making the subsequent reactions toward butadiene difficult as MgO lacks the acidic sites for aldol condensation reactions. As this strong adsorption of acetaldehyde is not observed for the Si/MgO catalyst, we propose that Si incorporation into the MgO domain could reduce the affinity of the intermediates on the catalyst surface and/or enable the subsequent reactions to butadiene (for example, aldol condensation and the dehydration of acetaldehyde and crotyl alcohol) by the cooperative interplay of acidic Si species in the basic MgO domain with



contributions from neighbouring hydroxy groups (Si–OH–Mg). This again highlights that the catalytic sites for the ethanol-to-butadiene pathway are not individual acidic and basic sites (and their physical mixtures; Fig. 4), but the synergy of acidic and basic sites in close proximity, created by wet kneading.

## Conclusions

Wet kneading is a non-conventional catalyst synthesis method, but essential for the preparation of active silica–magnesia catalysts for the one-step ethanol-to-butadiene process. The chemical changes that this preparation method elicits in the pristine SiO<sub>2</sub> and Mg(OH)<sub>2</sub> precursors, in particular, the nature of the magnesium silicates thought to be the active components, has long been unclear. We have demonstrated here that cross-deposition of Si and Mg species occurs on Mg(OH)<sub>2</sub> and SiO<sub>2</sub>, respectively, under wet-kneading conditions. Two model catalysts prepared by modified wet-kneading, that is, Si/MgO and Mg/SiO<sub>2</sub>, play different catalytic roles in the Lebedev process. More specifically, it is evident that the magnesium silicates on Si/MgO can be held responsible for butadiene formation, while the magnesium silicates on Mg/SiO<sub>2</sub> primarily produce ethylene. The close proximity of acidic and basic sites in Si–OH–Mg species in Si/MgO is thought to be key to efficient conversion, by lowering the activation energy of the multiple steps towards butadiene. To prove that, we developed a spectroscopic titration approach that revealed that the Si modification on MgO (Si/MgO) creates additional acid sites and that these sites are within 5 Å of the basic sites. We strongly believe that the spectroscopic approach developed here can be broadly applied to other catalytic systems where the distance between acidic and basic sites is relevant, such as other biomass conversion reactions<sup>100</sup>. Also, acid–acid proximity could be investigated as some catalytic reactions, such as the conversion of methanol to olefins<sup>101–103</sup> and the propene oligomerization<sup>104,105</sup>, have been proven to be sensitive to the location of Brønsted acid sites.

Apart from the improved rate of production of butadiene with the model Si/MgO catalyst, the insights provided here into the structural requirements for wet-kneaded silica–magnesia catalysts will aid in the development of next-generation Lebedev catalysts. A direct consequence of our study is that the source of the silica component can be revisited. In this and previous studies, expensive silica structures, such as Stöber silica, were used but, based on these results, the structure of the silica source is irrelevant and cheaper silica sources could be used as they will be dissolved and redispersed on MgO.

## Methods

### Catalyst synthesis

The wet-kneaded silica–magnesia catalysts were prepared from Stöber SiO<sub>2</sub> and Mg(OH)<sub>2</sub> precursors according to the published procedure<sup>17,21</sup>. The Stöber SiO<sub>2</sub> was prepared by hydrolysis of tetraethyl orthosilicate in a mixture of ethanol and ammonium hydroxide solution. After aging for 15 h, solid SiO<sub>2</sub> nanoparticles were obtained by rotary evaporation at reduced pressure. Mg(OH)<sub>2</sub> was synthesized by adding 0.4 M NaOH aqueous solution dropwise to 0.2 M Mg(NO<sub>3</sub>)<sub>2</sub> aqueous solution until the pH reached 12. The precipitated Mg(OH)<sub>2</sub> particles were separated by centrifugation and washed multiple times with deionized water. The as-prepared wet-kneading precursors were dried overnight in a convection oven at 120 °C. The dried precursors were then wet kneaded in deionized water (the nominal molar ratio of Si and Mg was 1.0 and the mass ratio of liquid to solid was 95.7 g/g) at room temperature for various wet-kneading times (10 min to 72 h). After wet kneading, the catalytic samples were obtained by centrifugation and dried overnight at 120 °C (the catalysts are named WK-time-dried, where time = 10 min to 72 h). Finally, the samples obtained after drying were calcined at 500 °C for 5 h at a heating rate of 5 °C min<sup>-1</sup> (denoted as WK-time-calc). For comparison, a physical mixture of SiO<sub>2</sub> and Mg(OH)<sub>2</sub> was prepared using a pestle and mortar for 10 min. The two model catalysts

(Mg/SiO<sub>2</sub> and Si/MgO) were prepared by modified wet-kneading for 72 h in 3 M ammonium nitrate and 7.3 M ammonium hydroxide aqueous solutions, respectively. The model catalysts were obtained by centrifugation, dried and calcined as described above. The loading of Mg and Si on SiO<sub>2</sub> and MgO was 2.6 and 9.8 wt%, respectively (determined by ICP-OES analysis). The pH of the wet-kneading medium was measured using a Mettler Toledo SevenMulti device with an InLab Expert PRO-ISM electrode.

### Inductively coupled plasma optical emission spectroscopy

Elemental analysis of Si and Mg was conducted on a 5100 ICP-OES instrument (Agilent) using argon as the carrier gas. Digestion was executed in a solution containing a mixture of hydrochloric acid, nitric acid and hydrofluoric acid (6:2:1 v/v/v ratio) at maximum settings of 273 °C and 35 bar on an UltraWAVE apparatus (Milestone).

### Scanning transmission electron microscopy combined with energy dispersive X-ray spectroscopy

HAADF-STEM analysis and EDX elemental mapping of the catalyst samples were performed with an FEI Titan G 2 80–300 kV electron microscope operated at 300 kV. Elemental maps were acquired using an electron beam current of 0.5 nA with an average time per single map of ~1 min. Quantitative EDX area profiles were calculated with 75 lines consisting of 25 pixels per line.

### Thermal gravimetric analysis

TGA measurements were performed using a Mettler Toledo TGA/DSC1 Star<sup>®</sup> system with a sample mass of ~15 mg. The heating programme was the same as that used for the calcination step under a continuous air flow of 20 ml min<sup>-1</sup>.

### Powder X-ray diffraction

PXRD patterns were acquired on a Bruker D8 Advance diffractometer operated at 40 kV and 40 mA using scanning monochromatic Cu K $\alpha$  radiation ( $\lambda = 1.5406$  Å) while applying a scan speed of 8 s per step and a step size of 0.03° over a 2 $\theta$  range of 5–80°. Crystalline phases were identified using the *Diffra.Eva* software with the help of the PDF-4+ (ref. 106) crystal database. The crystallite size of the catalysts was calculated using the Scherrer equation with a shape factor of 0.89 and an instrumental line broadening of 0.05° 2 $\theta$ . The experimental patterns were best fitted to the brucite (Mg(OH)<sub>2</sub>) crystal phase, exhibiting hexagonal settings and crystallizing in the P3m1 (#164) space group with unit cell parameters  $a = b = 3.1477$  Å,  $c = 4.7717$  Å,  $\alpha = \beta = 90^\circ$  and  $\gamma = 120^\circ$ . Pawley refinements were performed using the crystal data<sup>107</sup> for brucite (Mg(OH)<sub>2</sub>) with the help of Reflex in the Accelrys Material Studio software package. During the refinements, the unit cell parameters were adjusted, and the background and peak shape were modelled by a four-term polynomial and Pearson VII function, respectively. Other textural characteristics, such as the degree of crystallinity, were also analysed in Reflex (Accelrys) over the full measurement range. Because brucite has a lamellar structure with interlamellar distances coinciding with the  $c$  axis, the (001) diffraction line was evaluated when analysing the expansion and contraction of stacking spaces between (Mg(OH)<sub>2</sub>) <sub>$n$</sub>  sheets. The in situ temperature-programmed XRD measurement was performed on the Bruker D8 Advance system equipped with an Anton-Paar HTK1200N furnace. A 2 $\theta$  range of 35–70° was used with a step size of 0.02°. The PXRD patterns were collected every 10 °C, from 30 to 500 °C, with a ramp rate of 5 °C min<sup>-1</sup>. Each PXRD pattern was collected over a period of 1 min. The intensity of the crystalline phase was normalized on the basis of the maximum peak intensity of the (101) and (200) diffraction lines of brucite and periclase, respectively. The small diffractions in the in situ PXRD patterns were due to the alumina corundum XRD holder (Joint Committee of Powder Diffraction Standards database entry 46-1212, 2 $\theta = 25.6, 35.4, 37.8, 43.4, 52.6, 57.5$  and 66.6°).

## Nitrogen and argon physisorption

N<sub>2</sub> physisorption was measured at -196 °C using a Micromeritics ASAP 2420 high-throughput analysis system. Samples were outgassed at 300 °C under vacuum for 8 h. The specific surface areas were estimated according to the BET method in the relative pressure range ( $p/p_0$ ) of 0.05–0.95 (where  $p$  and  $p_0$  denote partial pressure of adsorbate gas in equilibrium at surface at the temperature of analysis and for saturated pressure of adsorbate at the temperature of analysis, respectively). Ar physisorption was performed at -186 °C using a Micromeritics ASAP 2040 system with the micropore option. Before the physisorption experiment, the samples were dried overnight at 350 °C under vacuum ( $p < 2 \mu\text{mHg}$ ) for 4 h and for an additional 2 h at 90 °C before the start of the micropore analysis (ramp rate 10 °C min<sup>-1</sup>). Using the low-pressure incremental dose mode up to a relative pressure of 0.01, samples were dosed with 7 ml g<sup>-1</sup> adsorptive per gram of sample. The BET-derived surface areas were calculated according to the Rouquerol criteria<sup>108</sup>. The microporous area and micropore volume were calculated using the Dubinin–Radushkevich method (MicroActive v4.00 software from Micromeritics). The pore size distribution was obtained using the SAIEUS v3.0 software, applying a density functional theory (DFT) model (Oxide-Ar-87, 2D NLDFT Heterogenous Surface) to the adsorption data. For the data fitting, values for regularization parameter ( $\lambda$ ) were set between 2.5 and 3, and the standard deviations of the fits were between 0.75 and 0.98.

## TPD using ammonia and carbon dioxide as probe molecules

The temperature-programmed desorption of NH<sub>3</sub> and CO<sub>2</sub> was performed on a Micromeritics ASAP 2920 unit. The samples were pretreated in a quartz reactor at 350 °C for 30 min and then cooled to 40 and 50 °C, respectively, in a flow of helium. Subsequently, NH<sub>3</sub> (10 vol% in He) and CO<sub>2</sub> (99.999%) were introduced to the catalyst for 15 min at 40 and 50 °C, respectively. Then the flow was switched to He for 15 min to remove physisorbed species from the catalyst surface. Finally, the samples were heated to 500 and 700 °C for NH<sub>3</sub> and CO<sub>2</sub>, respectively, and the desorption of NH<sub>3</sub> and CO<sub>2</sub> was measured using thermal conductivity and MS.

## DRIFTS and mass spectroscopy

The DRIFTS–MS study was performed on a Nicolet 6700 FTIR spectrometer equipped with a liquid nitrogen-cooled mercury–cadmium–telluride detector combined with an online gas-phase Transpector CPM mass spectrometer (1–100 AMU). He (>99.999%), which has no overlap with the main products or intermediates in the ethanol conversion, was used as the carrier gas. For the TPSR experiments, ~40 mg of sample was pretreated at 425 °C for 40 min in a flow of He (20 ml min<sup>-1</sup>) at a heating rate of 5 °C min<sup>-1</sup>. The samples were then cooled to 50 °C and loaded with ethanol for 30 min using He as the carrier gas. After that, the samples were purged with He for 30 min at 50 °C to eliminate the physically adsorbed ethanol. Then the ethanol TPSR experiment was performed by heating the sample from 50 to 500 °C at a heating rate of 5 °C min<sup>-1</sup> and then held at 500 °C for 30 min. For the in situ DRIFTS experiments, the same pretreatment procedure was adopted without the cooling step, and ethanol was continuously introduced at 425 °C. The in situ DRIFT spectra were obtained by subtracting the background spectrum of the bare catalyst after pretreatment, and information on the gas-phase ethanol was obtained by flowing ethanol through the cell loaded with KBr. The infrared data were processed by means of the Kubelka–Munk conversion using the OMNIC 8 software (version 8.2.0.387). The online gas-phase products were analysed by MS and compared with the contents of the National Institute of Standards and Technology database. The  $m/z$  values of the reactant and products were as follows: hydrogen (2), helium (4), water (17), ethylene (26 and 27), ethanol (31), butadiene (39 and 54), crotyl alcohol (57) and crotonaldehyde (70). Acetaldehyde is not specified in the MS results due to its complexity and potential overlap with other possible products, such

as  $m/z = 29$  (ethyl radical) and 44 (carbon dioxide). The chemisorption of the two probe molecules (NH<sub>3</sub> and CHCl<sub>3</sub>) was performed using the DRIFTS set-up. The samples were placed in the cell and pretreated before each experiment under a flow of He at 500 °C for 60 min (ramp rate 5 °C min<sup>-1</sup>). After cooling to 50 °C, a spectrum was collected and the sample treated in a flow of NH<sub>3</sub> (0.5% balanced with He, 10 ml min<sup>-1</sup>) for 30 min. To remove physisorbed NH<sub>3</sub>, the sample was purged with He (30 ml min<sup>-1</sup>) for 30 min. CHCl<sub>3</sub> was introduced to the sample in a flow of He (10 ml min<sup>-1</sup>) through a CHCl<sub>3</sub>-containing bubbler for 30 min. Similarly to NH<sub>3</sub>, the sample was further purged with He (30 ml min<sup>-1</sup>) for 30 min to remove physisorbed CHCl<sub>3</sub>. To prevent any contamination by water or oxygen, the samples in the DRIFTS cell were transferred in an argon glove box (both H<sub>2</sub>O and O<sub>2</sub> levels below 0.1 ppm).

## Solid-state NMR spectroscopy

Samples for the solid-state NMR experiments were ground and transferred to a 4 mm zirconia rotor. In situ <sup>29</sup>Si MAS NMR experiments were performed on a Bruker 400 MHz (9.4 T) wide-bore magnet with an AVANCE-III console equipped with a Bruker 4 mm HX MAS probe in <sup>1</sup>H and <sup>29</sup>Si double resonance mode. The experiments were performed at room temperature with a MAS frequency of 5 kHz. Note that the effective sample temperature can be 5–10 °C higher due to frictional heating. Hard <sup>29</sup>Si  $\pi/2$  pulses were applied with a field strength of 125 kHz, a 20 s recycle delay and an accumulation of 128 scans. The 1D <sup>1</sup>H–<sup>29</sup>Si CP MAS NMR spectra were recorded using a 5 s recycle delay, 28 ms acquisition time and 34,560 scans with a MAS frequency of 12 kHz. The 2D frequency-switched Lee–Goldberg <sup>1</sup>H–<sup>29</sup>Si HETCOR spectra were recorded using a 4 s recycle delay, 10 ms (direct dimension, F2) and 9.5 ms (indirect dimension, F1) acquisition times with an accumulation of 1,024 scans. During the CP step, <sup>1</sup>H CP spin-lock pulses centred at 38 kHz were linearly ramped from 75% to 100% and the <sup>29</sup>Si radiofrequency (RF) field was matched to obtain the optimal signal. <sup>1</sup>H and <sup>29</sup>Si chemical shifts were referenced externally to adamantane and hexamethylcyclotrioxane, respectively. For DNP SENS analysis, ~20 mg of sample was prepared by incipient wetness impregnation with 20  $\mu\text{l}$  of 16 mM TEKPol (Cortecnet) in 1,1,2,2-tetrachloroethane (TCE). TEKPol was dried under high vacuum (<10<sup>-4</sup> mbar) and TCE was stirred over calcium hydride and distilled in vacuo<sup>109</sup>. The DNP SENS spectra were acquired using a 300 GHz/400 MHz Avance III Bruker DNP solid-state NMR spectrometer equipped with a 3.2 mm Bruker triple-resonance low-temperature MAS probe. Experiments were performed at -100 K with 280 GHz gyrotron microwave irradiation. The sweep coil of the main magnetic field was set for microwave irradiation occurring at the <sup>1</sup>H positive enhancement maximum of the TEKPol biradical. One-dimensional <sup>1</sup>H–<sup>29</sup>Si DNP SENS spectra were collected with a 5 s recycle delay, 13 ms acquisition time and 64 scans with a 4 ms contact time at a MAS frequency of 8 kHz. The DNP enhancement factor ( $\epsilon$ ) was ~80 for each measurement. The <sup>29</sup>Si direct-excitation MAS NMR and natural-abundance <sup>25</sup>Mg NMR spectra were recorded on a Bruker 900 MHz (21.1 T) wide-bore magnet. The 1D <sup>29</sup>Si direct-excitation MAS NMR spectrum was recorded using a 3.2 mm HX probe with a 20 s recycle delay at a MAS frequency of 20 kHz. The 1D <sup>25</sup>Mg direct-excitation MAS NMR spectrum was recorded using a 4 mm HX low-gamma probe with a 0.5 s recycle delay, 30 ms acquisition time and accumulation of 1,024 scans at a MAS frequency of 10 kHz. The 2D <sup>25</sup>Mg  $z$ -filtered 3Q MAS NMR spectra<sup>110</sup> were recorded using a 0.5 s recycle delay with 7,200 scans with 50  $\mu\text{s}$  t<sub>1</sub> (where t<sub>1</sub> denotes time-domain increments) at a MAS frequency of 10 kHz. The optimized pulse widths for excitation, conversion and central-transition selective pulses were 15, 5.3 and 40  $\mu\text{s}$ , respectively. The  $z$ -filter delay between the conversion and the selective pulse was 20  $\mu\text{s}$ . Before Fourier transformation, the 1D and 2D NMR spectra were processed using an exponential window and a  $\pi/3$ -shifted squared sine-bell window in the F1 dimension, respectively. The 3Q MAS data were processed with a shearing transformation available in Bruker Topspin software (v3.6.3). The Haeberlen convention

was used to describe the chemical shift tensor in terms of the isotropic shift ( $\delta_{\text{iso}} = (\delta_{xx} + \delta_{yy} + \delta_{zz})/3$ ) and chemical shift anisotropy (CSA) shift asymmetric parameter ( $\eta_{\text{CSA}} = (\delta_{yy} - \delta_{xx})/(\delta_{zz} - \delta_{\text{iso}})$ ) with the principal components ordered as follows:  $|\delta_{zz} - \delta_{\text{iso}}| \geq |\delta_{xx} - \delta_{\text{iso}}| \geq |\delta_{yy} - \delta_{\text{iso}}|$ . The quadrupolar tensor is described by the nuclear quadrupolar coupling constant ( $C_Q = eQV_{zz}/h$ ) and quadrupolar asymmetric parameter ( $\eta_Q = (V_{xx} - V_{yy})/V_{zz}$ ), where  $e$  is the electric charge,  $Q$  is the nuclear quadrupole moment,  $V$  is the electric field gradient and  $h$  is Planck's constant. The  $^{25}\text{Mg}$  QCPMG, DFS-QCPMG and  $^1\text{H}$ - $^{25}\text{Mg}$  CP-QCPMG experiments were performed at a MAS frequency of 10 kHz or under static conditions. Typically, the QCPMG pulse sequence was obtained using a 1 s recycle delay and 40  $\mu\text{s}$  central-transition  $\pi$ -refocusing selective pulse with 50  $\mu\text{s}$  spin-echo delays<sup>111</sup>. During the DFS pulse, the RF was linearly swept for 4 ms from 300 to 100 kHz. The  $^1\text{H}$ - $^{25}\text{Mg}$  CP-QCPMG experiments were performed with a 10 ms contact time after optimization using  $\text{Mg}(\text{OH})_2$ . The 1D  $^{25}\text{Mg}$  QCPMG, DFS-QCPMG and CP-QCPMG spectra were apodized using Lorentzian line broadening of 20 Hz. The 1D  $^{25}\text{Mg}$  DFS-QCPMG and 2D 3Q MAS NMR spectra were fitted using the WSolids1 (version 1.21.3) and DMFIT (version dmfit 20200306)<sup>112</sup> software, respectively. The  $^{25}\text{Mg}$  chemical shifts were externally referenced to  $\text{MgCl}_2$  at 0 ppm. The solid-state  $^1\text{H}$  DQ-SQ MAS NMR experiments were performed on a Bruker 600 MHz (14.1 T) wide-bore magnet with a MAS frequency of 20 kHz using a back-to-back recoupling sequence with two rotor periods for the excitation and reconversion of double-quantum coherences with a duration of 100  $\mu\text{s}$ . The corresponding solid-state NMR samples were prepared in a 3.2 mm zirconia rotor in an argon glove box.

### Catalytic activity test

All catalytic reactions were conducted in an Avantium four-channel Flowrence XD high-throughput reactor system at 425 °C and ambient pressure<sup>21</sup>. To ensure that the reactions were not performed in a heat transfer limitation regime, a very diluted ethanol feed in nitrogen carrier gas (2.2 vol/vol%) was used. The catalyst bed was diluted with silicon carbide in a catalyst/SiC volume ratio of 1:4 to decrease the effect of axial dispersion and to improve heat conduction in the bed. Typically, 50  $\mu\text{l}$  catalyst was mixed with 200  $\mu\text{l}$  grit46 SiC and placed in a quartz tube with an internal diameter of 2.3 mm. The LHSV (liquid flow volume per hour and per catalyst volume) was varied in nitrogen carrier gas. The absence of internal and external mass transfer limitation was verified by using the Weisz-Prater criterion and by using a constant LHSV with a fixed amount of catalyst, respectively (Supplementary Note 6 and Supplementary Fig. 27). The unreacted ethanol and reaction products were analysed by gas chromatography (GC) using an Agilent 7890B gas chromatograph equipped with three detectors (two flame ionization detectors (FID) and one thermal conductivity detector (TCD)). The FID channels were equipped with a 10 m precolumn with a wax stationary phase and a 30 m Gaspro stationary phase to separate ethanol, acetaldehyde,  $\text{C}_1$ - $\text{C}_7$  hydrocarbons and oxygenates. The TCD channel contained a PoraPLOT Q GC, a HayeSep Q and a Molsieve for the analytical column. The conversion of ethanol ( $X$ ) and product selectivities ( $S_i$ ) were calculated using the following formulae:

$$X = \frac{C_{\text{EtOH}_{\text{in}}} - C_{\text{EtOH}_{\text{out}}}}{C_{\text{EtOH}_{\text{in}}}} \times 100 \quad (1)$$

$$S_i = \frac{i \times C_i}{2(C_{\text{EtOH}_{\text{in}}} - C_{\text{EtOH}_{\text{out}}})} \times 100 \quad (2)$$

where  $C_{\text{EtOH}_{\text{in}}}$  and  $C_{\text{EtOH}_{\text{out}}}$  are the concentrations of ethanol in the blank and reactor, respectively,  $i$  is the number of carbons in product  $i$  and  $C_i$  is the concentration of product  $i$ , determined by GC analysis. Note that there were no alcohols or any other oxygenates in the detected  $\text{C}_4$ - $\text{C}_7$  hydrocarbons.

### Data availability

The data supporting the findings of this article are available in the paper and its Supplementary Information or from the corresponding author on reasonable request.

### References

1. Bruijninx, P. C. A. & Weckhuysen, B. M. Shale gas revolution: an opportunity for the production of biobased chemicals? *Angew. Chem. Int. Ed.* **52**, 11980–11987 (2013).
2. Angelici, C., Weckhuysen, B. M. & Bruijninx, P. C. A. Chemocatalytic conversion of ethanol into butadiene and other bulk chemicals. *ChemSusChem* **6**, 1595–1614 (2013).
3. Makshina, E. V. et al. Review of old chemistry and new catalytic advances in the on-purpose synthesis of butadiene. *Chem. Soc. Rev.* **43**, 7917–7953 (2014).
4. Pomalaza, G., Arango Ponton, P., Capron, M. & Dumeignil, F. Ethanol-to-butadiene: the reaction and its catalysts. *Catal. Sci. Technol.* **10**, 4860–4911 (2020).
5. Bin Samsudin, I., Zhang, H., Jaenicke, S. & Chuah, G. K. Recent advances in catalysts for the conversion of ethanol to butadiene. *Chem. Asian J.* **15**, 4199–4214 (2020).
6. Jones, M. D. Catalytic transformation of ethanol into 1,3-butadiene. *Chem. Cent. J.* **8**, 53 (2014).
7. Pomalaza, G., Capron, M., Ordonsky, V. & Dumeignil, F. Recent breakthroughs in the conversion of ethanol to butadiene. *Catalysts* **6**, 203 (2016).
8. Dussol, D., Cadran, N., Laloue, N., Renaudot, L. & Schweitzer, J.-M. M. New insights of butadiene production from ethanol: elucidation of concurrent reaction pathways and kinetic study. *Chem. Eng. J.* **391**, 123586 (2020).
9. Li, F. et al. Cooperative  $\text{CO}_2$ -to-ethanol conversion via enriched intermediates at molecule-metal catalyst interfaces. *Nat. Catal.* **3**, 75–82 (2020).
10. Wang, X. et al. Efficient electrically powered  $\text{CO}_2$ -to-ethanol via suppression of deoxygenation. *Nat. Energy* **5**, 478–486 (2020).
11. Wang, Y. et al. Direct conversion of  $\text{CO}_2$  to ethanol boosted by intimacy-sensitive multifunctional catalysts. *ACS Catal.* **11**, 11742–11753 (2021).
12. Cabello González, G. M. et al. Ethanol conversion into 1,3-butadiene over a mixed Hf-Zn catalyst: effect of reaction conditions and water content in ethanol. *Fuel Process. Technol.* **193**, 263–272 (2019).
13. Angelici, C., Velthoen, M. E. Z., Weckhuysen, B. M. & Bruijninx, P. C. A. Influence of acid-base properties on the Lebedev ethanol-to-butadiene process catalyzed by  $\text{SiO}_2$ -MgO materials. *Catal. Sci. Technol.* **5**, 2869–2879 (2015).
14. Natta, G. & Rigamonti, R. Studio roentgenografico e chimico dei catalizzatori usati per la produzione del butadiene dall'alcool. *Chim. Ind.* **29**, 239–243 (1947).
15. Kvisle, S., Aguero, A. & Sneed, R. P. A. Transformation of ethanol into 1,3-butadiene over magnesium oxide/silica catalysts. *Appl. Catal.* **43**, 117–131 (1988).
16. Janssens, W. et al. Ternary Ag/MgO-SiO<sub>2</sub> catalysts for the conversion of ethanol into butadiene. *ChemSusChem* **8**, 994–1008 (2015).
17. Chung, S.-H. et al. Role of magnesium silicates in wet-kneaded silica-magnesia catalysts for the Lebedev ethanol-to-butadiene process. *ACS Catal.* **6**, 4034–4045 (2016).
18. Angelici, C., Velthoen, M. E. Z., Weckhuysen, B. M. & Bruijninx, P. C. A. Effect of preparation method and CuO promotion in the conversion of ethanol into 1,3-butadiene over  $\text{SiO}_2$ -MgO catalysts. *ChemSusChem* **7**, 2505–2515 (2014).
19. Li, S. et al. Morphological control of inverted MgO-SiO<sub>2</sub> composite catalysts for efficient conversion of ethanol to 1,3-butadiene. *Appl. Catal. A* **577**, 1–9 (2019).



20. Huang, X., Men, Y., Wang, J., An, W. & Wang, Y. Highly active and selective binary MgO–SiO<sub>2</sub> catalysts for the production of 1,3-butadiene from ethanol. *Catal. Sci. Technol.* **7**, 168–180 (2017).
21. Chung, S. et al. The importance of thermal treatment on wet-kneaded silica–magnesia catalyst and Lebedev ethanol-to-butadiene process. *Nanomaterials* **11**, 579 (2021).
22. Yi, H. et al. A novel method for surface wettability modification of talc through thermal treatment. *Appl. Clay Sci.* **176**, 21–28 (2019).
23. Lewandowski, M. et al. Investigations into the conversion of ethanol to 1,3-butadiene using MgO:SiO<sub>2</sub> supported catalysts. *Catal. Commun.* **49**, 25–28 (2014).
24. Taifan, W. E., Bučko, T. & Baltrusaitis, J. Catalytic conversion of ethanol to 1,3-butadiene on MgO: a comprehensive mechanism elucidation using DFT calculations. *J. Catal.* **346**, 78–91 (2017).
25. Taifan, W. E. & Baltrusaitis, J. In situ spectroscopic insights on the molecular structure of the MgO/SiO<sub>2</sub> catalytic active sites during ethanol conversion to 1,3-butadiene. *J. Phys. Chem. C.* **122**, 20894–20906 (2018).
26. Zhang, T., Cheeseman, C. R. & Vandeperre, L. J. Development of low pH cement systems forming magnesium silicate hydrate (M-S-H). *Cem. Concr. Res.* **41**, 439–442 (2011).
27. Tonelli, M. et al. Structural characterization of magnesium silicate hydrate: towards the design of eco-sustainable cements. *Dalton Trans.* **45**, 3294–3304 (2016).
28. Nied, D., Enemark-Rasmussen, K., L'Hopital, E., Skibsted, J. & Lothenbach, B. Properties of magnesium silicate hydrates (M-S-H). *Cem. Concr. Res.* **79**, 323–332 (2016).
29. Cole, W. F. A crystalline hydrated magnesium silicate formed in the breakdown of a concrete sea-wall. *Nature* **171**, 354–355 (1953).
30. Roos, C. et al. Crystal structure of magnesium silicate hydrates (M-S-H): the relation with 2:1 Mg–Si phyllosilicates. *Cem. Concr. Res.* **73**, 228–237 (2015).
31. Sindorf, D. & Maciel, G. Cross-polarization magic-angle-spinning silicon-29 nuclear magnetic resonance study of silica gel using trimethylsilane bonding as a probe of surface geometry and reactivity. *J. Phys. Chem.* **86**, 5208–5219 (1982).
32. Leonardelli, S., Facchini, L., Fretigny, C., Tougen, P. & Legrand, A. P. Silicon-29 NMR study of silica. *J. Am. Chem. Soc.* **114**, 6412–6418 (1992).
33. Kobayashi, T., Perras, F. A., Slowing, I. I., Sadow, A. D. & Pruski, M. Dynamic nuclear polarization solid-state NMR in heterogeneous catalysis research. *ACS Catal.* **5**, 7055–7062 (2015).
34. Magi, M., Lippmaa, E., Samoson, A., Engelhardt, G. & Grimmer, A. R. Solid-state high-resolution silicon-29 chemical shifts in silicates. *J. Phys. Chem.* **88**, 1518–1522 (1984).
35. Moravetski, V., Hill, J.-R., Eichler, U., Cheetham, A. K. & Sauer, J. <sup>29</sup>Si NMR chemical shifts of silicate species: ab initio study of environment and structure effects. *J. Am. Chem. Soc.* **118**, 13015–13020 (1996).
36. Pustovgar, E. et al. Understanding silicate hydration from quantitative analyses of hydrating tricalcium silicates. *Nat. Commun.* **7**, 10952 (2016).
37. Szabó, B. et al. MgO–SiO<sub>2</sub> catalysts for the ethanol to butadiene reaction: the effect of Lewis acid promoters. *ChemCatChem* **12**, 5686–5696 (2020).
38. Walling, S. A., Kinoshita, H., Bernal, S. A., Collier, N. C. & Provis, J. L. Structure and properties of binder gels formed in the system Mg(OH)<sub>2</sub>–SiO<sub>2</sub>–H<sub>2</sub>O for immobilisation of Magnox sludge. *Dalton Trans.* **44**, 8126–8137 (2015).
39. Bernard, E. et al. Characterization of magnesium silicate hydrate (M-S-H). *Cem. Concr. Res.* **116**, 309–330 (2019).
40. Salomão, R., Arruda, C. C. & Antunes, M. L. P. Synthesis, dehydroxylation and sintering of porous Mg(OH)<sub>2</sub>–MgO clusters: evolution of microstructure and physical properties. *Interceram. Int. Ceram. Rev.* **69**, 52–62 (2020).
41. van Aken, P. A. & Langenhorst, F. Nanocrystalline, porous periclase aggregates as product of brucite dehydration. *Eur. J. Mineral.* **13**, 329–341 (2001).
42. Gomez-Villalba, L. S., Sierra-Fernandez, A., Rabanal, M. E. & Fort, R. TEM-HRTEM study on the dehydration process of nanostructured Mg–Ca hydroxide into Mg–Ca oxide. *Ceram. Int.* **42**, 9455–9466 (2016).
43. Rollinson, H. & Adetunji, J. in *Encyclopedia of Geochemistry: A Comprehensive Reference Source on the Chemistry of the Earth* (ed White, W. M.) 738–743 (Springer, 2018); [https://doi.org/10.1007/978-3-319-39312-4\\_340](https://doi.org/10.1007/978-3-319-39312-4_340)
44. Shannon, R. D. Revised effective ionic radii and systematic studies of interatomic distances in halides and chalcogenides. *Acta Crystallogr. Sect. A* **32**, 751–767 (1976).
45. Green, J. Calcination of precipitated Mg(OH)<sub>2</sub> to active MgO in the production of refractory and chemical grade MgO. *J. Mater. Sci.* **18**, 637–651 (1983).
46. Litasov, K. D. & Ohtani, E. in *Advances in High-Pressure Mineralogy* Vol. 421 (ed Ohtani, E.) 115–156 (Geological Society of America, 2007).
47. Lippmaa, E., Mägi, M., Samoson, A., Engelhardt, G. & Grimmer, A. R. Structural studies of silicates by solid-state high-resolution <sup>29</sup>Si NMR. *J. Am. Chem. Soc.* **102**, 4889–4893 (1980).
48. MacKenzie, K. J. D., Bradley, S., Hanna, J. V. & Smith, M. E. Magnesium analogues of aluminosilicate inorganic polymers (geopolymers) from magnesium minerals. *J. Mater. Sci.* **48**, 1787–1793 (2013).
49. Chabrol, K. et al. Functionalization of synthetic talc-like phyllosilicates by alkoxyorganosilane grafting. *J. Mater. Chem.* **20**, 9695–9706 (2010).
50. Mackenzie, K. J. D. & Meinhold, R. H. Thermal reactions of chrysotile revisited: a <sup>29</sup>Si and <sup>25</sup>Mg MAS NMR study. *Am. Mineral.* **79**, 43–50 (1994).
51. Stebbins, J. F., Smyth, J. R., Panero, W. R. & Frost, D. J. Forsterite, hydrous and anhydrous wadsleyite and ringwoodite (Mg<sub>2</sub>SiO<sub>4</sub>): <sup>29</sup>Si NMR results for chemical shift anisotropy, spin-lattice relaxation, and mechanism of hydration. *Am. Mineral.* **94**, 905–915 (2009).
52. Temuujin, J., Okada, K. & MacKenzie, K. J. D. Role of water in the mechanochemical reactions of MgO–SiO<sub>2</sub> systems. *J. Solid State Chem.* **138**, 169–177 (1998).
53. d'Espinose de la Caillerie, J.-B., Kermarec, M. & Clause, O. <sup>29</sup>Si NMR observation of an amorphous magnesium silicate formed during impregnation of silica with Mg(II) in aqueous solution. *J. Phys. Chem.* **99**, 17273–17281 (1995).
54. Hartman, J. S. & Millard, R. L. Gel synthesis of magnesium silicates: a <sup>29</sup>Si magic angle spinning NMR study. *Phys. Chem. Miner.* **17**, 1–8 (1990).
55. Benhelal, E. et al. Insights into chemical stability of Mg-silicates and silica in aqueous systems using <sup>25</sup>Mg and <sup>29</sup>Si solid-state MAS NMR spectroscopy: applications for CO<sub>2</sub> capture and utilisation. *Chem. Eng. J.* **420**, 127656 (2021).
56. Freitas, J. C. C. & Smith, M. E. Recent advances in solid-state <sup>25</sup>Mg NMR spectroscopy. *Annu. Rep. NMR Spectrosc.* **75**, 25–114 (2012).
57. Pallister, P. J., Moudrakovski, I. L. & Ripmeester, J. A. Mg-25 ultra-high field solid state NMR spectroscopy and first principles calculations of magnesium compounds. *Phys. Chem. Chem. Phys.* **11**, 11487–11500 (2009).
58. Blanc, F., Middlemiss, D. S., Gan, Z. & Grey, C. P. Defects in doped LaGaO<sub>3</sub> anionic conductors: linking NMR spectral features, local environments, and defect thermodynamics. *J. Am. Chem. Soc.* **133**, 17662–17672 (2011).

59. Jäger, C., Kunath, G., Losso, P. & Scheler, G. Determination of distributions of the quadrupole interaction in amorphous solids by  $^{27}\text{Al}$  satellite transition spectroscopy. *Solid State Nucl. Magn. Reson.* **2**, 73–82 (1993).
60. Hatakeyama, M., Nemoto, T., Kanehashi, K. & Saito, K. Natural abundance solid-state  $^{25}\text{Mg}$  MQMAS NMR studies on inorganic solids at a high magnetic field of 16.4 T. *Chem. Lett.* **34**, 864–865 (2005).
61. Hayashi, Y. et al. Experimental and computational studies of the roles of MgO and Zn in talc for the selective formation of 1,3-butadiene in the conversion of ethanol. *Phys. Chem. Chem. Phys.* **18**, 25191–25209 (2016).
62. Chierigato, A. et al. On the chemistry of ethanol on basic oxides: revising mechanisms and intermediates in the Lebedev and Guerbet reactions. *ChemSusChem* **8**, 377–388 (2015).
63. Sushkevich, V. L. & Ivanova, I. I. Mechanistic study of ethanol conversion into butadiene over silver promoted zirconia catalysts. *Appl. Catal. B* **215**, 36–49 (2017).
64. Gruver, V., Sun, A. & Fripiat, J. J. Catalytic properties of aluminated sepiolite in ethanol conversion. *Catal. Lett.* **34**, 359–364 (1995).
65. Velasquez Ochoa, J., Malmusi, A., Recchi, C. & Cavani, F. Understanding the role of gallium as a promoter of magnesium silicate catalysts for the conversion of ethanol into butadiene. *ChemCatChem* **9**, 2128–2135 (2017).
66. Taifan, W. E., Yan, G. X. & Baltrusaitis, J. Surface chemistry of MgO/SiO<sub>2</sub> catalyst during the ethanol catalytic conversion to 1,3-butadiene: in-situ DRIFTS and DFT study. *Catal. Sci. Technol.* **7**, 4648–4668 (2017).
67. Taifan, W. E. *Catalytic Transformation of Ethanol to 1,3-Butadiene over MgO/SiO<sub>2</sub> Catalyst*. PhD thesis, Lehigh University (2018).
68. Klein, A., Keisers, K. & Palkovits, R. Formation of 1,3-butadiene from ethanol in a two-step process using modified zeolite- $\beta$  catalysts. *Appl. Catal. A* **514**, 192–202 (2016).
69. Szabó, B. et al. Conversion of ethanol to butadiene over mesoporous In<sub>2</sub>O<sub>3</sub>-promoted MgO-SiO<sub>2</sub> catalysts. *Mol. Catal.* **491**, 110984 (2020).
70. Karkanas, P., Bar-Yosef, O., Goldberg, P. & Weiner, S. Diagenesis in prehistoric caves: the use of minerals that form in situ to assess the completeness of the archaeological record. *J. Archaeol. Sci.* **27**, 915–929 (2000).
71. Lide, D. R. & Haynes, W. M. *CRC Handbook of Chemistry and Physics: A Ready-Reference Book of Chemical and Physical Data: 2009–2010* (ed Lide, D. R.) 90th edn (CRC Press, 2009).
72. Iler, R. K. *The Chemistry of Silica: Solubility, Polymerization, Colloid and Surface Properties and Biochemistry of Silica* (Wiley, 1979).
73. Ayrál, A. et al. Silica membranes—basic principles. *Period. Polytech. Chem. Eng.* **50**, 67–79 (2006).
74. Kim, H. N. & Lee, S. K. Atomic structure and dehydration mechanism of amorphous silica: insights from  $^{29}\text{Si}$  and  $^1\text{H}$  solid-state MAS NMR study of SiO<sub>2</sub> nanoparticles. *Geochim. Cosmochim. Acta* **120**, 39–64 (2013).
75. Alba, M. D., Becerro, A. I., Castro, M. A. & Perdígón, A. C. High-resolution  $^1\text{H}$  MAS NMR spectra of 2:1 phyllosilicates. *Chem. Commun.* 37–38 (2000).
76. Schnell, I. & Spiess, H. W. High-resolution  $^1\text{H}$  NMR spectroscopy in the solid state: very fast sample rotation and multiple-quantum coherences. *J. Magn. Reson.* **151**, 153–227 (2001).
77. Yarulina, I. et al. Structure–performance descriptors and the role of Lewis acidity in the methanol-to-propylene process. *Nat. Chem.* **10**, 804–812 (2018).
78. Ochoa, J. V. et al. An analysis of the chemical, physical and reactivity features of MgO–SiO<sub>2</sub> catalysts for butadiene synthesis with the Lebedev process. *Green Chem.* **18**, 1653–1663 (2016).
79. Singh, M., Zhou, N., Paul, D. K. & Klabunde, K. J. IR spectral evidence of aldol condensation: acetaldehyde adsorption over TiO<sub>2</sub> surface. *J. Catal.* **260**, 371–379 (2008).
80. Moteki, T. & Flaherty, D. W. Mechanistic insight to C–C bond formation and predictive models for cascade reactions among alcohols on Ca- and Sr-hydroxyapatites. *ACS Catal.* **6**, 4170–4183 (2016).
81. Alabugin, I. V., Bresch, S. & dos Passos Gomes, G. Orbital hybridization: a key electronic factor in control of structure and reactivity. *J. Phys. Org. Chem.* **28**, 147–162 (2015).
82. Ochoa, J. V., Malmusi, A., Recchi, C. & Cavani, F. Understanding the role of gallium as a promoter of magnesium silicate catalysts for the conversion of ethanol into butadiene. *ChemCatChem* **9**, 2128–2135 (2017).
83. Tsuchida, T. et al. Reaction of ethanol over hydroxyapatite affected by Ca/P ratio of catalyst. *J. Catal.* **259**, 183–189 (2008).
84. Díez, V. K., Apesteguía, C. R. & Di Cosimo, J. I. Acid-base properties and active site requirements for elimination reactions on alkali-promoted MgO catalysts. *Catal. Today* **63**, 53–62 (2000).
85. Di Cosimo, J. I., Díez, V. K., Xu, M., Iglesia, E. & Apesteguía, C. R. Structure and surface and catalytic properties of Mg–Al basic oxides. *J. Catal.* **178**, 499–510 (1998).
86. Kozłowski, J. T. & Davis, R. J. Heterogeneous catalysts for the Guerbet coupling of alcohols. *ACS Catal.* **3**, 1588–1600 (2013).
87. Gines, M. J. L. & Iglesia, E. Bifunctional condensation reactions of alcohols on basic oxides modified by copper and potassium. *J. Catal.* **176**, 155–172 (1998).
88. Birky, T. W., Kozłowski, J. T. & Davis, R. J. Isotopic transient analysis of the ethanol coupling reaction over magnesia. *J. Catal.* **298**, 130–137 (2013).
89. Abdulrazzaq, H. T., Rahmani Chokanlu, A., Frederick, B. G. & Schwartz, T. J. Reaction kinetics analysis of ethanol dehydrogenation catalyzed by MgO–SiO<sub>2</sub>. *ACS Catal.* **10**, 6318–6331 (2020).
90. Qi, L. et al. Ethanol conversion to butadiene over isolated zinc and yttrium sites grafted onto dealuminated beta zeolite. *J. Am. Chem. Soc.* **142**, 14674–14687 (2020).
91. Idriss, H., Diagne, C., Hindermann, J. P., Kiennemann, A. & Barteau, M. A. Reactions of acetaldehyde on CeO<sub>2</sub> and CeO<sub>2</sub>-supported catalysts. *J. Catal.* **155**, 219–237 (1995).
92. Guil, J. M., Homs, N., Llorca, J. & Ramírez de la Piscina, P. Microcalorimetric and infrared studies of ethanol and acetaldehyde adsorption to investigate the ethanol steam reforming on supported cobalt catalysts. *J. Phys. Chem. B* **109**, 10813–10819 (2005).
93. Chavez Diaz, C. D., Locatelli, S. & Gonzo, E. E. Acetaldehyde adsorption on HZSM-5 studied by infrared spectroscopy. *Zeolites* **12**, 851–857 (1992).
94. Yan, T. et al. Mechanistic insights into one-step catalytic conversion of ethanol to butadiene over bifunctional Zn–Y/beta zeolite. *ACS Catal.* **8**, 2760–2773 (2018).
95. Hemelsoet, K. et al. Experimental and theoretical IR study of methanol and ethanol conversion over H-SAPO-34. *Catal. Today* **177**, 12–24 (2011).
96. Aronson, M. T., Gorte, R. J. & Farneth, W. E. An infrared spectroscopy study of simple alcohols adsorbed on H-ZSM-5. *J. Catal.* **105**, 455–468 (1987).
97. Sushkevich, V. L., Ivanova, I. I., Ordonsky, V. V. & Taarning, E. Design of a metal-promoted oxide catalyst for the selective synthesis of butadiene from ethanol. *ChemSusChem* **7**, 2527–2536 (2014).
98. Fan, D., Dong, X., Yu, Y. & Zhang, M. A DFT study on the aldol condensation reaction on MgO in the process of ethanol to 1,3-butadiene: understanding the structure–activity relationship. *Phys. Chem. Chem. Phys.* **19**, 25671–25682 (2017).

99. Dong, X., Liu, C., Fan, D., Yu, Y. & Zhang, M. Insight into the effect of promoters (M = Cu, Ag, Zn, Zr) on aldol condensation reaction based on MgO surface in the process of ethanol to 1,3-butadiene: a comparative DFT study. *Appl. Surf. Sci.* **481**, 576–587 (2019).
100. Sudarsanam, P. et al. Functionalised heterogeneous catalysts for sustainable biomass valorisation. *Chem. Soc. Rev.* **47**, 8349–8402 (2018).
101. Deimund, M. A. et al. Effect of heteroatom concentration in SSZ-13 on the methanol-to-olefins reaction. *ACS Catal.* **6**, 542–550 (2016).
102. Gallego, E. M. et al. Making nanosized CHA zeolites with controlled Al distribution for optimizing methanol-to-olefin performance. *Chem. Eur. J.* **24**, 14631–14635 (2018).
103. Di Iorio, J. R., Nimlos, C. T. & Gounder, R. Introducing catalytic diversity into single-site chabazite zeolites of fixed composition via synthetic control of active site proximity. *ACS Catal.* **7**, 6663–6674 (2017).
104. Bernauer, M. et al. Proton proximity—new key parameter controlling adsorption, desorption and activity in propene oligomerization over H-ZSM-5 zeolites. *J. Catal.* **344**, 157–172 (2016).
105. Tabor, E., Bernauer, M., Wichterlová, B. & Dedecek, J. Enhancement of propene oligomerization and aromatization by proximate protons in zeolites: FTIR study of the reaction pathway in ZSM-5. *Catal. Sci. Technol.* **9**, 4262–4275 (2019).
106. Gates-Rector, S. & Blanton, T. The Powder Diffraction File: a quality materials characterization database. *Powder Diffr.* **34**, 352–360 (2019).
107. Černý, R., Valvoda, V. & Chládek, M. Empirical texture corrections for asymmetric diffraction and inclined textures. *J. Appl. Crystallogr.* **28**, 247–253 (1995).
108. Rouquerol, J., Llewellyn, P. & Rouquerol, F. in *Studies in Surface Science and Catalysis* Vol. 160 (ed Llewellyn, P. L.) 49–56 (Elsevier, 2007).
109. Dutta Chowdhury, A., Yarulina, I., Abou-Hamad, E., Gurinov, A. & Gascon, J. Surface enhanced dynamic nuclear polarization solid-state NMR spectroscopy sheds light on Brønsted–Lewis acid synergy during the zeolite catalyzed methanol-to-hydrocarbon process. *Chem. Sci.* **10**, 8946–8954 (2019).
110. Amoureux, J. P., Fernandez, C. & Steuernagel, S. Z filtering in MQMAS NMR. *J. Magn. Reson. A* **123**, 116–118 (1996).
111. Larsen, F. H., Skibsted, J., Jakobsen, H. J. & Nielsen, N. C. Solid-state QCPMG NMR of low- $\gamma$  quadrupolar metal nuclei in natural abundance. *J. Am. Chem. Soc.* **122**, 7080–7086 (2000).
112. Massiot, D. et al. Modelling one- and two-dimensional solid-state NMR spectra. *Magn. Reson. Chem.* **40**, 70–76 (2002).
- E. Kaliyamoorthy for ICP-OES analysis, S. Lopatin for TEM–EDX measurements, C. Canlas for technical support in recording solid-state NMR spectra, Y. Yuan for in situ PXRD measurements and K. Eichele (Universität Tübingen) for WSolids1 software support. The preliminary experiments in this research were performed within the framework of the CatchBio programme. B.M.W. and P.C.A.B. acknowledge the support of the Smart Mix Program of the Netherlands Ministry of Economic Affairs, the Netherlands Ministry of Education, Culture and Science, and NWO (Middelgroot programme, grant no. 700.58.102).

## Author contributions

S.-H.C. and J.R.-M. conceived the research and directed the project. S.-H.C. designed the experiments and analysed the data. T.L. and A.R. collected and processed the DRIFTS–MS spectra and catalytic activity test results, respectively. T.S., S.K., I.M., G.S., S.T., A.D., E.A.-H., X.T. and P.L. characterized the prepared catalysts under the guidance of S.-H.C., J.G. and J.R.-M. B.S. conducted preliminary experiments for the catalyst synthesis under the supervision of B.M.W. and P.C.A.B. S.-H.C. and J.R.-M. co-wrote the paper. All authors discussed the results and commented on different versions of the manuscript.

## Competing interests

The authors declare no competing interests.

## Additional information

**Supplementary information** The online version contains supplementary material available at <https://doi.org/10.1038/s41929-023-00945-0>.

**Correspondence and requests for materials** should be addressed to Sang-Ho Chung or Javier Ruiz-Martínez.

**Peer review information** *Nature Catalysis* thanks Attila Domján and the other, anonymous, reviewer(s) for their contribution to the peer review of this work.

**Reprints and permissions information** is available at [www.nature.com/reprints](http://www.nature.com/reprints).

**Publisher's note** Springer Nature remains neutral with regard to jurisdictional claims in published maps and institutional affiliations.

Springer Nature or its licensor (e.g. a society or other partner) holds exclusive rights to this article under a publishing agreement with the author(s) or other rightsholder(s); author self-archiving of the accepted manuscript version of this article is solely governed by the terms of such publishing agreement and applicable law.

© The Author(s), under exclusive licence to Springer Nature Limited 2023, corrected publication 2023

## Acknowledgements

The authors are grateful for financial support from King Abdullah University of Science and Technology. We thank J. Vittenet and